terminal bronchioles (Fig. 1a, b). The EHTB lesions were independently localized from the DHPN-induced alveolar cell hyperplastic lesions (Fig. 1c). The incidences and multiplicity (number/cm^2 lung tissue section) of EHTB in the groups treated with nZnO were significantly increased compared with that of the DHPN alone group. The increase was dose-dependent (Spearman rank correlation test, $p < 0.001$) (Table 1). Immunostaining with proliferating cell nuclear antigen (PCNA) indicated that proliferating bronchiolar epithelial cells were preferentially found in the EHTB lesions, but rarely found in the normal terminal bronchial epithelial areas (Fig. 1d, e).

Another lesion found in the groups treated with nZnO, and also independent of DHPN treatment, was interstitial pneumonitis (Fig. 2a). The lesion was usually associated with fibrosis of various thicknesses of the septal wall extruding into the alveolar structure (blue staining in Fig. 2b). Quantitative analysis indicated a significant increase in the fibrotic area in the rats treated with nZnO compared with that of rats treated with DHPN alone (Fig. 2c), and the increase was dose-dependent (Spearman rank correlation test, $p < 0.001$). In addition, the EHTB lesions often occurred near or within interstitial pneumonitis areas.

Light microscopic observation of the alveoli of the rats treated with nZnO showed infiltration of numerous macrophages mixed with a few neutrophils, eosinophils, and lymphocytes (data not shown). The nZnO particles were not found in any of the alveolar macrophages; these macrophages contained numerous vacuolar vesicles in the cytoplasm (Fig. 2d). Transmission electron microscopic (TEM) observation showed that nZnO particles were not found within the vacuolar vesicles (Fig. 2e) or in any alveolar tissue cells (Fig. 2f). The absence of a zinc peak was confirmed by elemental scanning with TEM-X-ray microanalysis (Figure S2). nZnO particles were also not detected under polarized light microscope observation. This feature was in contrast with titanium dioxide nanoparticles which were clearly observed in alveolar macrophages (Figure S3).

Reversibility of EHTB and FAIP in wild-type rats

As in the H*ras*128 transgenic rats, nZnO induced EHTB and FAIP in wild-type Sprague–Dawley (SD) rats (Fig. 3a), and nZnO was not found in the lung tissue. nZnO-induced EHTB and FAIP gradually regressed with time (Fig. 3a), and the number of EHTB foci per square centimeter lung tissue section decreased from 9.81 ± 1.42 at day 1 to 0.06 ± 0.13 at week 12 after cessation of nZnO exposure (Fig. 3b). The total Zn^{2+} content in the lung tissue also gradually decreased (Fig. 3c) and was positively correlated with the number of EHTB ($r = 0.96$ by Pearson correlation test).

Microarray analysis

Microarray analysis of the lung tissue indicated that nZnO treatment up-regulated the expression of 738 genes and down-regulated the expression of 267 genes (data not shown). The up-regulated inflammation-associated genes included chemotactic chemokines such as Cxcl5, Cxcl11, Ccl7, Cxcl2, Ccl2, and Cxcl1, proinflammatory cytokines such as Tnfa and Il6, and the acute-phase reactant Orm1 (Table S1). Pathway analysis showed an increase in inflammatory responses in which macrophages and TNFα play a central role (Figure S4). The gene expression profiling was consistent with the strong inflammatory responses in the lung observed by histological examination. Other pathways up-regulated by nZnO included classical complement activation pathway, matrix metalloproteinase pathway, cholesterol biosynthesis pathway and striated muscle contraction pathway, and treatment of nZnO down-regulated the adipogenesis pathway (data not shown).

Effects of $ZnCl_2$ solution on the lung of wild-type rats

To check whether the nZnO-induced EHTB and FAIP were due to dissolution of nZnO to Zn^{2+}, we administered $ZnCl_2$ solution (the molecular amount is equal to that of 500 μg/ml nZnO suspension) to the lung of rats by IPS. The lesions were histologically similar to those observed in the nZnO-treated rats (Fig. 4a, b, c). Quantitative analysis of EHTB indicated that the number of EHTB induced by $ZnCl_2$ solution and nZnO was comparable (Fig. 4d).

To examine whether Zn^{2+} and nZnO have the same underlying molecular mechanisms, two genes, Tnfa and Orm1, which were determined to be up-regulated in the nZnO-treated rats by microarray analysis, were chosen for gene expression analysis. These genes were chosen because Tnfa-encoded tumor necrosis factor alpha is a multifunctional proinflammatory cytokine involved in a variety of acute and chronic inflammatory responses, and Orm1-encoded alpha 1 acid glycoprotein (AGP) is an acute-phase protein usually synthesized by hepatocytes in response to trauma, infection, and inflammation (Fournier et al. 2000). RT-PCR (Fig. 4e) and real-time PCR (Fig. 4f) showed that treatment with both $ZnCl_2$ solution and nZnO increased the expression of Tnfa and Orm1 genes in the lung tissue, with a little higher induction in the $ZnCl_2$ solution treated rats. Similarly, increased expression of Orm1 genes was found in primary alveolar macrophages exposed to nZnO in vitro (Fig. 4g). Interestingly, addition of human AGP to nZnO suspension dose-dependently promoted dissolution of nZnO from 59.1 nmol/ml (19.7 % dissolved,

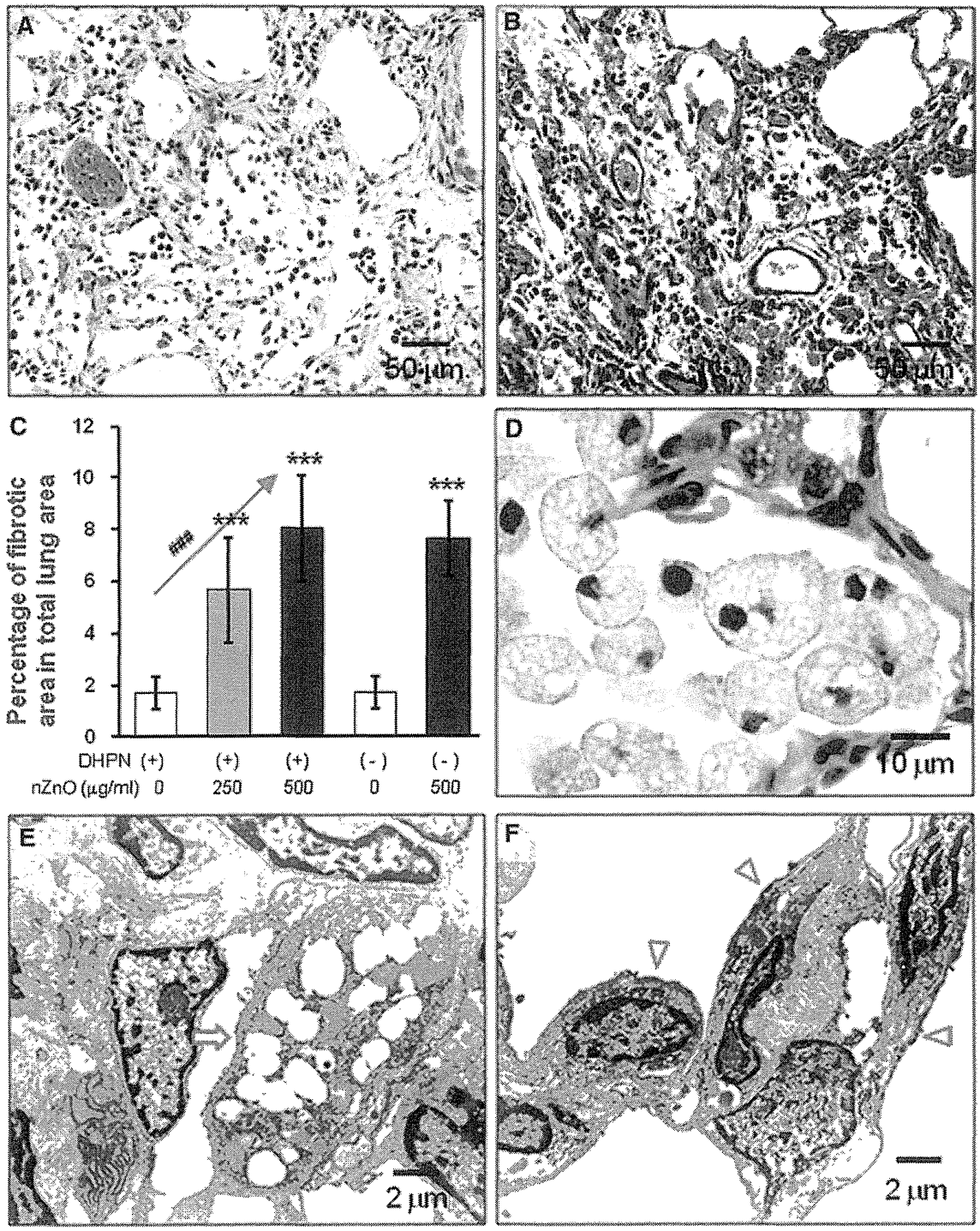

Fig. 2 Induction of FAIP and observation of nZnO particles. **a** representative image of FAIP in rats treated with nZnO; **b** image of Azan–Mallory staining in the lung of rats treated with nZnO, showing collagen fibers; **c** percentage of the fibrotic area in total lung tissue area. ***<0.001 by two-tailed Student's *t*-test versus the vehicle group; and ###$p < 0.001$ by Spearman rank correlation test. **d** image showing alveolar macrophages with vacuous phagocytosis vesicles; **e** and **f** TEM images showing alveolar macrophages (*arrow*) and epithelium (*arrow heads*), no nZnO particles being observed

without addition of AGP) to 117.3 nmol/ml (39.1 % dissolved after addition of 500 μg/ml of AGP), while addition of bovine serum albumin (BSA) had little effect on dissolution of nZnO (Fig. 4h). Exposure of both nZnO and $ZnCl_2$ solution resulted in dose-dependent cell death in vitro (Figure S5).

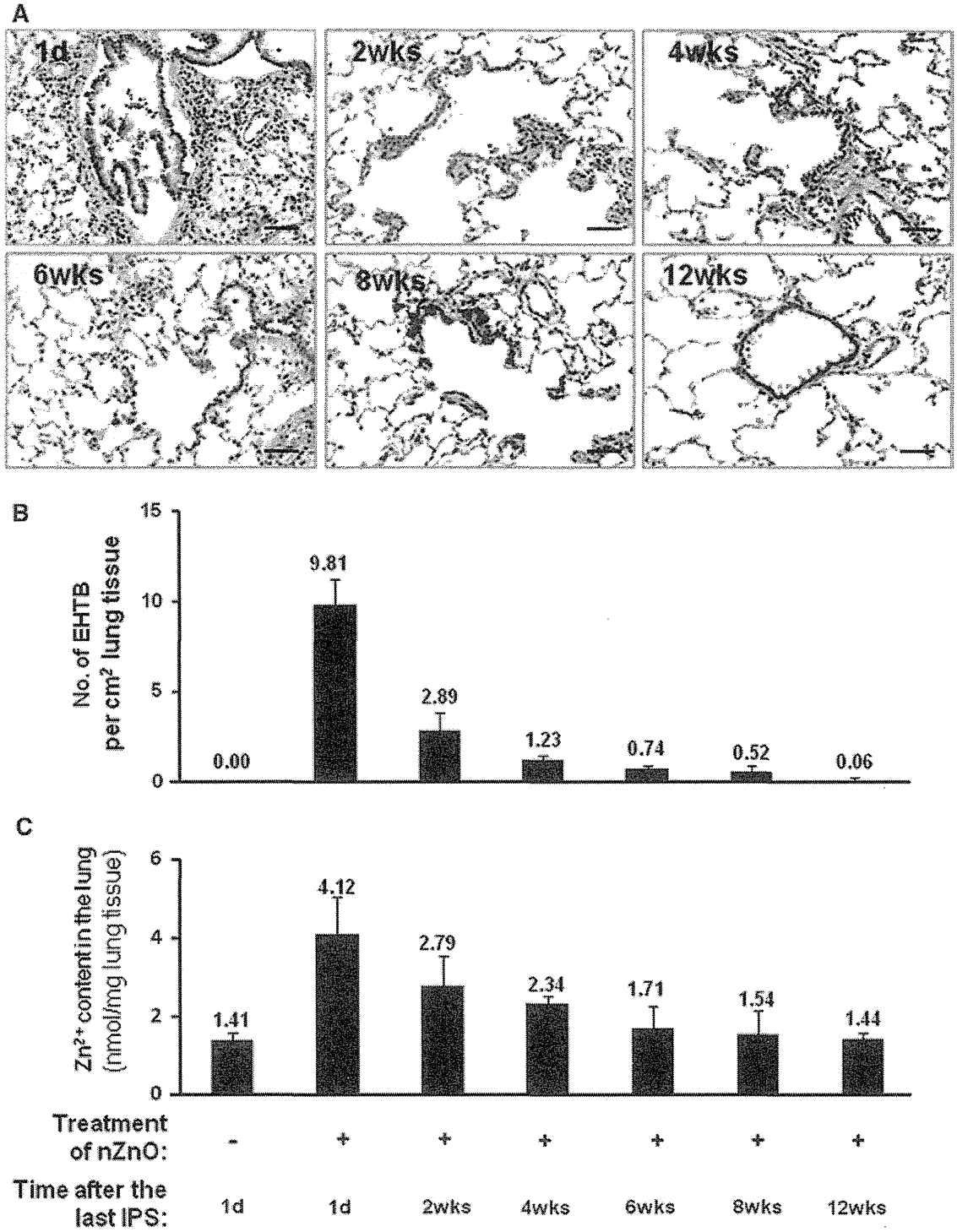

Fig. 3 nZnO-induced EHTB and FAIP are reversible. Wild-type rats were treated with 500 μg/ml nZnO by IPS 2 times/week for 4 weeks and killed at different time points of 1 day (1d) and 2, 4, 6, 8, and 12 weeks (wks) after the last IPS. **a** histological images of the lung tissues; **b** number of EHTB per cm^2 lung tissue and **c** Zn^{2+} content in the lung tissues at different time points. *Bars* = 50 μm

Effects of nZnO particles and $ZnCl_2$ solution on other organs and serum of wild-type rats

Obvious lesions and macrophages containing vacuolar vesicles were not found in other major organs including the liver, kidney, spleen, or brain by histological examination (data not shown). The results of blood cell examination are shown in Table S2: The only changes were increased proportions of monocytes and eosinophils that were rapidly recovered within 2 weeks post exposure. Biochemical

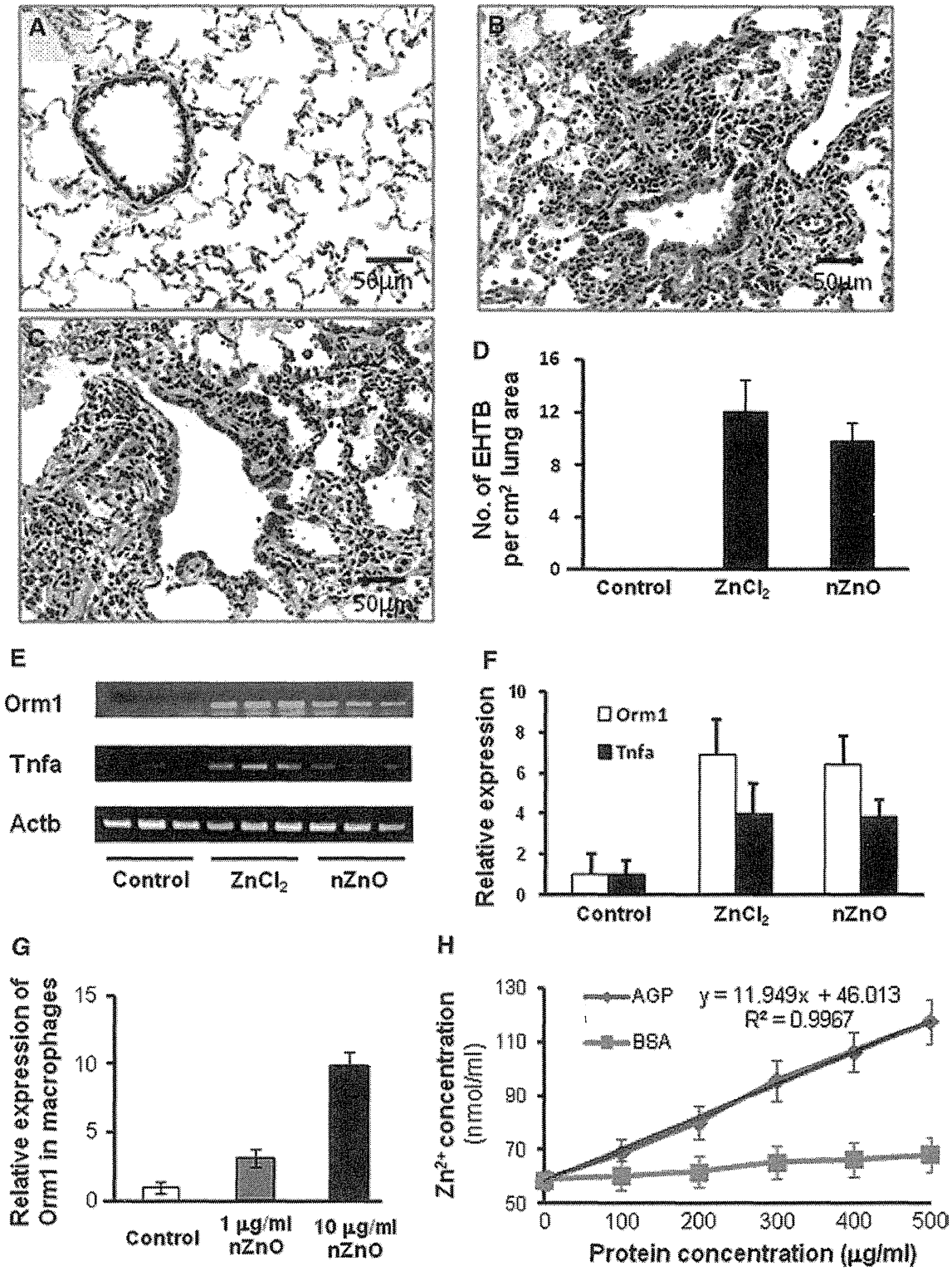

Fig. 4 Similar effects of $ZnCl_2$ solution and nZnO in induction of EHTB and FAIP in wild-type rats. **a** H&E-stained slides of the lungs of rats treated with vehicle; **b** with nZnO; and **c** with $ZnCl_2$ solution, showing EHTB and FAIP; **d** comparable number of EHTB per square centimeter of the lung tissues induced by treatment of $ZnCl_2$ and nZnO; **e** gene expression determined by RT-PCR of Orm1 and Tnfa, with Actb gene as an internal control; **f** real-time PCR analysis of gene expression of Orm1 and Tnfa, which was normalized with Actb expression; **g** induction of Orm1 expression in primary alveolar macrophages exposed to nZnO; and **h** effect of human alpha 1 acid glycoprotein (AGP) and bovine serum albumin (BSA) on dissolution of nZnO in vitro

examination of serum markers for tissue and organ injuries indicated no significant changes compared to the vehicle group (Table S3). Administration of nZnO or $ZnCl_2$ to the lung led to a transient increase in serum Zn^{2+} concentration which returned to normal levels within 2 weeks after administration. The elevated serum Zn^{2+} did not affect the homeostasis of the other ions examined (Table S4).

Discussion

In vivo nanomaterial toxicity usually implicates oxidative stress, inflammation (Nel et al. 2006), and other biological responses depending on the individual nanomaterial. In vitro assays related to carcinogenicity, such as mammalian cell transformation and gene mutation assays, cannot represent the complex in vivo processes of different biological alterations and are not always suitable for risk assessment of nanomaterial carcinogenicity. In the present study, we tested the carcinogenic activity of nZnO in H*ras*128 rats by an initiation–promotion protocol, by which we previously found promotion effect of nanosized titanium dioxide on DHPN-induced lung and mammary carcinogenesis (Xu et al. 2010). nZnO did not show any promotion effects on lung proliferative or neoplastic lesions, indicating that nZnO is not carcinogenetic. Also, nZnO did not promote DHPN-induced mammary carcinogenesis.

On the other hand, nZnO was found to induce EHTB in H*ras*128 rats and wild-type SD rats. EHTB is a proliferative lesion of the terminal bronchiolar epithelium. It should be noted that the localization of EHTB was independent from that of DHPN-induced alveolar cell hyperplasia. This observation clearly indicates that the DHPN-induced alveolar cell hyperplasia and EHTB have different etiology, the latter being induced by nZnO. We also observed 2 cases of alveolar cell hyperplasia out of 6 cases in the nZnO alone group. This is not significant and thus considered to be spontaneous or an inflammation-associated event. The EHTB lesions regressed when administration of nZnO was discontinued and completely disappeared after 12 weeks. Along with EHTB, the interstitial inflammatory changes often observed surrounding the EHTB lesions also regressed. Our data and other reports (Cho et al. 2011) indicate that the EHTB lesions do not progress directly to cancers but are reactive proliferation associated with inflammatory events. Similar reversible inflammatory changes in the bronchoalveolar lavage fluids by administration of nanoscale or fine ZnO particles via inhalation or intratracheal instillation have previously been reported (Warheit et al. 2009).

nZnO particles were not found in alveolar macrophages, in the lung tissue, or in other organs, suggesting that the particles were dissolved to Zn^{2+}. Accordingly, we conducted experiments to determine whether Zn^{2+} would induce similar lesions. $ZnCl_2$ solution induced closely similar lung lesions and gene expression profiles as nZnO, demonstrating that the observed lung lesions were caused by Zn^{2+}. This was confirmed by increased Zn^{2+} level in the lung and serum after administration of nZnO. Interestingly, treatment with nZnO up-regulated the expression of the Omr1 gene in both the lung and the alveolar macrophages, and in vitro addition of Omr1-encoded AGP dose-dependently promoted nZnO dissolution. After Zn^{2+} was cleared from the lung, the EHTB and FAIP lesions disappeared, and this was evidenced by the positive correlation of EHTB number with Zn^{2+} content in the lung. Dissolution of nZnO has been reported to be particle size- and pH-dependent (Mudunkotuwa et al. 2012). Increased Omr1 expression possibly alters the microenvironment of the alveolar macrophages and the lung which accelerates nZnO dissolution. The elevated Zn^{2+} from nZnO dissolution possibly interferes with zinc ion homeostasis and leads to cytotoxic effects (Kao et al. 2012).

According to OSHA, the permissible exposure limit for zinc oxide particles is 15 mg/m^3 of air for total dust and 5 mg/m^3 for the respirable fraction (http://www.osha.gov/SLTC/healthguidelines/zincoxide/recognition.html). The inhalation exposure limit per kilogram of body weight per day for the respirable fraction is 192 μg, calculated from 6,000 ml of minute respiratory volume and 8 working hours for a 75 kg body weight worker. The dosing in the carcinogenesis study of the present study was approximately 35.5 and 71 μg/kg body weight a day (calculated from 125 to 250 μg every two weeks for a 250 g rat) and is lower than the OSHA limit for humans. Since nZnO has more potential to be ionized than larger ZnO particles because of its higher surface area (Mudunkotuwa et al. 2012), this feature should be taken into regulatory consideration.

It has been estimated that engineered nanomaterials will become a $1 trillion enterprise by 2015 (Nel et al. 2006), and ensuring health and environmental safety is a challenging task to the nanotechnology industry. Among numerous engineered nanomaterials, metal based or carbon based, most of which have been shown to have toxic effects to at least some extent, nZnO is a promising nanomaterial for biomedical applications. The results of the present study indicate that, although nZnO induced reversible lung toxicity, it did not cause carcinogenic or chronic progressive inflammatory lesions. Also, since it is biodegradable to ions, nZnO is easily cleared from the body (Rasmussen et al. 2010). Our study also suggests that the toxic effects of nZnO can be further decreased if efforts such as proper dosing and surface coating are made to lower the Zn^{2+} release from nZnO.

In conclusion, treatment of nZnO by IPS did not promote lung and mammary carcinogenesis in our carcinogenesis model. Although nZnO induced EHTB and FAIP, the lesions regressed rapidly along with clearance of surplus Zn^{2+} from the lung and serum. Thus, from a toxicological viewpoint, under the present experimental conditions, exposure of the lung to nZnO does not cause progressive neoplastic development or chronic fibrosis in the lung. These findings will be helpful in evaluating of the safety of nZnO used in biomedical applications, in which its use is of rather short duration, although long-term studies including inhalation studies are required to assess their occupational and environmental health hazards.

Acknowledgments This work was supported by Health and Labor Sciences Research Grants (Research on Risk of Chemical Substance 21340601, H21-kagaku-ippan-008, H24-kagaku-ippan-009 and H22-kagaku-ippan-005) from the Ministry of Health, Labor and Welfare, Japan. We thank A. Iezaki for her excellent secretarial assistance for the work.

Conflict of interest The authors declare that they have no conflict of interest.

References

Antonini JM, Lewis AB, Roberts JR, Whaley DA (2003) Pulmonary effects of welding fumes: review of worker and experimental animal studies. Am J Ind Med 43:350–360

Baldwin S, Odio MR, Haines SL, O'Connor RJ, Englehart JS, Lane AT (2001) Skin benefits from continuous topical administration of a zinc oxide/petrolatum formulation by a novel disposable diaper. J Eur Acad Dermatol Venereol 15(Suppl 1):5–11

Cho WS, Duffin R, Howie SE, Scotton CJ, Wallace WA, Macnee W, Bradley M, Megson IL, Donaldson K (2011) Progressive severe lung injury by zinc oxide nanoparticles; the role of Zn2+ dissolution inside lysosomes. Part Fibre Toxicol 8:27–43

Deng X, Luan Q, Chen W, Wang Y, Wu M, Zhang H, Jiao Z (2009) Nanosized zinc oxide particles induce neural stem cell apoptosis. Nanotechnology 20:115101

Drinker CK, Fairhall LT (1933) Zinc in relation to general and industrial hygiene. Public Health Rep 48:955–961

Fine JM, Gordon T, Chen LC, Kinney P, Falcone G, Beckett WS (1997) Metal fume fever: characterization of clinical and plasma IL-6 responses in controlled human exposures to zinc oxide fume at and below the threshold limit value. J Occup Environ Med 39:722–726

Fournier T, Medjoubi NN, Porquet D (2000) Alpha-1-acid glycoprotein. Biochim Biophys Acta 1482:157–171

Heinrich U, Fuhst R, Rittinghausen S, Creutzenberg O, Bellmann B, Koch K, Levsen K (1995) Chronic inhalation exposure of wistar rats and two different strains of mice to diesel engine exhaust, carbon black, and titanium dioxide. Inhalation Toxicol 7:533–556

Hughes G, McLean NR (1988) Zinc oxide tape: a useful dressing for the recalcitrant finger-tip and soft-tissue injury. Arch Emerg Med 5:223–227

Hull MJ, Abraham JL (2002) Aluminum welding fume-induced pneumoconiosis. Hum Pathol 33:819–825

Kao YY, Chen YC, Cheng TJ, Chiung YM, Liu PS (2012) Zinc oxide nanoparticles interfere with zinc ion homeostasis to cause cytotoxicity. Toxicol Sci 125:462–472

Kermanizadeh A, Gaiser BK, Hutchison GR, Stone V (2012) An in vitro liver model–assessing oxidative stress and genotoxicity following exposure of hepatocytes to a panel of engineered nanomaterials. Part Fibre Toxicol 9:28

Lee J, Kang BS, Hicks B, Chancellor TF Jr, Chu BH, Wang HT, Keselowsky BG, Ren F, Lele TP (2008) The control of cell adhesion and viability by zinc oxide nanorods. Biomaterials 29:3743–3749

Mudunkotuwa IA, Rupasinghe T, Wu CM, Grassian VH (2012) Dissolution of ZnO nanoparticles at circumneutral pH: a study of size effects in the presence and absence of citric acid. Langmuir 28:396–403

Nel A, Xia T, Madler L, Li N (2006) Toxic potential of materials at the nanolevel. Science 311:622–627

Rasmussen JW, Martinez E, Louka P, Wingett DG (2010) Zinc oxide nanoparticles for selective destruction of tumor cells and potential for drug delivery applications. Expert Opin Drug Deliv 7:1063–1077

Sano T (1963) Pathology and pathogenesis of pneumoconiosis. Acta Pathol Jpn 13:77–93

Sayes CM, Reed KL, Warheit DB (2007) Assessing toxicity of fine and nanoparticles: comparing in vitro measurements to in vivo pulmonary toxicity profiles. Toxicol Sci 97:163–180

Tsuda H, Fukamachi K, Ohshima Y, Ueda S, Matsuoka Y, Hamaguchi T, Ohnishi T, Takasuka N, Naito A (2005) High susceptibility of human c-Ha-ras proto-oncogene transgenic rats to carcinogenesis: a cancer-prone animal model. Cancer Sci 96:309–316

Valdiglesias V, Costa C, Kilic G, Costa S, Pasaro E, Laffon B, Teixeira JP (2013) Neuronal cytotoxicity and genotoxicity induced by zinc oxide nanoparticles. Environ Int 55:92–100

Warheit DB, Sayes CM, Reed KL (2009) Nanoscale and fine zinc oxide particles: can in vitro assays accurately forecast lung hazards following inhalation exposures? Environ Sci Technol 43:7939–7945

Xia T, Kovochich M, Liong M, Madler L, Gilbert B, Shi H, Yeh JI, Zink JI, Nel AE (2008) Comparison of the mechanism of toxicity of zinc oxide and cerium oxide nanoparticles based on dissolution and oxidative stress properties. ACS Nano 2:2121–2134

Xu J, Futakuchi M, Iigo M, Fukamachi K, Alexander DB, Shimizu H, Sakai Y, Tamano S, Furukawa F, Uchino T, Tokunaga H, Nishimura T, Hirose A, Kanno J, Tsuda H (2010) Involvement of macrophage inflammatory protein 1 alpha (MIP 1 alpha) in promotion of rat lung and mammary carcinogenic activity of nanoscale titanium dioxide particles administered by intra-pulmonary spraying. Carcinogenesis 31:927–935

Yang H, Liu C, Yang D, Zhang H, Xi Z (2009) Comparative study of cytotoxicity, oxidative stress and genotoxicity induced by four typical nanomaterials: the role of particle size, shape and composition. J Appl Toxicol 29:69–78

J Toxicol Pathol 2013; 26: 335–341

Review

Colon Preneoplastic Lesions in Animal Models

Masumi Suzui[1*], Takamitsu Morioka[2], and Naoki Yoshimi[3]

[1] Department of Molecular Toxicology, Graduate School of Medical Sciences and Medical School, Nagoya City University, 1 Kawasumi, Mizuho-ku, Mizuho-cho, Nagoya 467-8601, Japan
[2] Radiation Effect Accumulation and Prevention Project, Fukushima Project Headquarters and Radiobiology for Children's Health Program, Research Center for Radiation Protection, National Institute of Radiological Sciences, 4-9-1 Anagawa, Inage-ku, Chiba 263-8555, Japan
[3] Department of Pathology and Oncology, Graduate School of Medicine and Faculty of Medicine, University of the Ryukyus Faculty of Medicine, 207 Uehara, Nishihara-cho, Okinawa 903-0215, Japan

Abstract: The animal model is a powerful and fundamental tool in the field of biochemical research including toxicology, carcinogenesis, cancer therapeutics and prevention. In the carcinogenesis animal model system, numerous examples of preneoplastic lesions have been isolated and investigated from various perspectives. This may indicate that several options of endpoints to evaluate carcinogenesis effect or therapeutic outcome are presently available; however, classification of preneoplastic lesions has become complicated. For instance, these lesions include aberrant crypt foci (ACF), dysplastic ACF, flat ACF, β-catenin accumulated crypts, and mucin-depleted foci. These lesions have been induced by commonly used chemical carcinogens such as azoxymethane (AOM), 1,2-dimethylhydrazine (DMH), methylnitrosourea (MUN), or 2-amino-1-methyl-6-phenylimidazo[4,5-*b*]pyridine (PhIP). Investigators can choose any procedures or methods to examine colonic preneoplastic lesions according to their interests and the objectives of their experiments. Based on topographical, histopathological, and biological features of colon cancer preneoplastic lesions in the animal model, we summarize and discuss the character and implications of these lesions. (DOI: 10.1293/tox.2013-0028; J Toxicol Pathol 2013; 26: 335–341)

Key words: preneoplastic lesion, colon carcinogenesis, animal model, topographic view

Aberrant Crypt Foci (ACF)

Bird[1] first reported in 1987 that when C57BL/6J mice were treated with azoxymethane (AOM), aberrant dysplastic crypts appeared in the colonic mucosa. After fixation with 10% buffered formalin and staining with methylene blue, these crypts were easily visualized in the topographic view of the colonic mucosa using a x4 objective (Fig. 1A). These lesions were referred to as aberrant crypts (AC) or aberrant crypt foci (ACF) in the colon of both animals and humans[2–4]. ACF were cryptic lesions distinguished by their increased size, thicker epithelial lining, and increased pericryptic zone[1]. ACF have only been seen in the colon of carcinogen-treated mice and rats. They have not been seen in the colon treated with a noncarcinogen or in untreated animals[2,3]. After carcinogen treatment, they appeared as early as within 2 weeks and persisted until the experimental termination of animals (16 weeks); histological changes from mild atypia to dysplasia[2] were also revealed. Two heterocyclic amines, 2-amino-3-methylimidazo[4,5-*f*]quinoline (IQ) and 2-amino-1-methyl-6-phenylimidazo[4,5-*b*]pyridine (PhIP), were shown to be able to induce ACF in the colon, respectively, after 4 and 10 weeks of exposure[5]. The number of ACF increased significantly over time, and small-sized ACF were predominant at all time points[5]. In histological slides, the large ACF exhibits dysplasia and thus can be termed a microadenoma[2].

ACF are also induced in the colonic mucosa of rats or mice treated with carcinogens such as AOM, methylazoxymethanol (MAM) acetate, 1,2-dimethylhydrazine (DMH), methylnitrosourea (MNU), PhIP, IQ, 2-amino-3,8-dimethylimidazo[4,5-*f*]quinoline (MeIQ) and 2-amino-6-methyldipyrido[1,2-*a*:3',2'-*d*]imidazole (Glu-P-1)[3,6–11]. In our previous experiments[7,12], F344 rats were subcutaneously (sc) injected with AOM (20 mg/kg body weight) twice. Five weeks after the beginning of the experiment, 93–139 ACF per colon occurred. When F344 rats were treated with AOM (15 mg/kg body weight, sc injection) 3 times, 240 ACF/colon occurred at 11 weeks after the beginning of the experiment[13]. When F344 rats were treated with DMH (40 mg/kg body weight, sc injection) twice, 175–200 ACF/colon were induced at 5 or 8 weeks after the beginning of the experiment[11,14,15]. These ACF usually contained 1–3 or more crypts per focus. The diameter of an aberrant crypt measured at least 3 to 4 times larger than that of a normal crypt

Received: 28 May 2013, Accepted: 27 June 2013
*Corresponding author: M Suzui (suzui@med.nagoya-cu.ac.jp)

in mice[2,16] and up to 1.5 times larger than a normal crypt in humans[17]. Pretlow *et al.*[16] reported that ACF were at least 3 times larger in diameter than normal crypts, and most ACF had lumina that were oval or slit shaped rather than circular. ACF range in size and have from 1 to 412 aberrant crypts per focus[17–20]. The size in the topographic view and the histologically dysplastic character of ACF are critical factors when we distinguish ACF as preneoplastic lesions. We consider that large ACF consisting of more than 10–20 crypts and manifesting dysplasia could be termed a microadenoma. In mouse models, for instance, B57BL/6J and CF_1 mice were given a single intraperitoneal (ip) injection of AOM (5 mg/kg body weight), and 4 weeks later, mice developed 2.6 and 3 ACF per colon, respectively[2]. BALB/c mice were ip injected with AOM (10 mg/kg body weight) twice, and 14 ACF were induced 4 weeks after the injection[21]. In C57BL/6J-*Min*/+ (*Min*) and C57BL/6J-+/+ (wild type) mice, PhIP was ip injected 4 times. Ten weeks after the injection, male mice developed 3 and 0 ACF, respectively, and female mice developed 1.9 and 0.2 ACF in their colons[22]. These findings indicate that duration of the experimental period, strain of animals, method of administration of carcinogens, and nature of carcinogen used as an initiator, may affect the number of ACF in the colonic mucosa.

In terms of the distribution of ACF, McLellan *et al.*[2] demonstrated that AOM-treated CF_1 mice developed ACF, 67% of which were in the rectal segment, 29% of which were in the middle segment and 4% of which were in the cecal segment. ACF were seen mainly in the rectal and middle segments when the animals were treated with DMH, NMU, MeIQ, or Glu-P-1[3]. Most ACF were found in the middle and distal colon in F344 rats treated with AOM[23]. In contrast, Hata *et al.*[24] demonstrated that ACF were frequently found in the proximal colon (cecal segment of the colon) when AKR/J and SWR/J mice were treated with AOM. The carcinogen IQ also induced ACF primarily in the middle and cecal segments of the colon[3]. Colon tumors induced by AOM were primarily found in distal colon rather than in proximal colon in the rat and mouse models[24,25], indicating that the correlation between ACF formation and carcinogenesis is not necessarily straightforward. This is presumably because of the heterogeneous nature of ACF[26–28]. Also, experimental protocol and species used may affect the difference in distribution of ACF[3,29–31].

The shape of the lumen of the ACF is relates to the histology of the ACF. Histological criteria of rat/mouse ACF have been described by several investigators[26,32]. Accordingly, ACF may be classified into the following 3 categories. In brief, these are (1) non dysplastic foci, which exhibit hypercellularity of uniform or normal looking goblet cells with basal-oriented nuclei and apical localization of mucus; (2) mild to moderate dysplastic foci, which exhibit hypercellularity of cells with elongated nuclei and focal nuclear stratification; and (3) moderate to severe dysplastic foci, which exhibit hypercellularity of elongated cells with abundant basophilic cytoplasm. These foci display enlarged and vesiculated nuclei, sometimes with prominent nucleoli.

Dysplastic ACF

The dysplastic nature of ACF was described by McLellan and Bird[2]. In a hematoxylin-eosin (HE) stained transverse section, ACF exhibited a focal appearance and mild cellular atypia, and dysplasia was observed in the large focus. Bird and Pretlow mentioned that use of the term dysplastic crypt foci to describe abnormal crypts is valid only if the investigators examined histologically all of the methylene blue-identified lesions and found dysplasia in all of them[33]. Ochiai *et al.*[34,35] described two distinct types of ACF in the PhIP-induced rat model. One was dysplastic ACF, and the other was nondysplastic ACF. In their reports, dysplastic ACF are histologically characterized by distortion of the crypt structure, a decrease in goblet cell number, existence of nuclear stratification, and enlarged nuclei. Nondysplastic ACF indicated the hyperplastic change in crypts. One-fourth of PhIP-induced ACF were dysplastic ACF, and the remaining ACF were nondysplastic ACF. Two-week dietary administration of 400 ppm PhIP was repeated three times with a 4-week interval. The average number of dysplastic ACF was up to 0.8 per colon, and they were larger in size than nondysplastic ACF after 32 weeks of experimentation. In the dysplastic ACF, cytoplasmic β-catenin protein accumulation and β-catenin gene mutation were found. The mutations were $^{32}A \rightarrow G$ (Asp→Gly), $^{34}G \rightarrow T$ (Gly→Val), and $^{36}C \rightarrow T$ (His→Tyr)[35]. By a staining method that uses 70% methanol followed by 0.2% methylene blue staining, dysplastic ACF can be topographically contrasted with nondysplastic ACF on the colonic mucosa and identified without performing histological examination[34]. The average number of dysplastic ACF/colon was 2.0–3.2 in F344 rats treated with PhIP (400 ppm in diet), MeIQ (300 ppm in diet), and IQ (300 ppm in diet). Two-week dietary administration of PhIP, MeIQ, or IQ was repeated three times with a 4-week interval. Other investigators[26,32,34,36] have also described dysplastic ACF. Thorup[32] found that a correlation between degree of dysplasia and crypt multiplicity, indicating that chemically induced ACF can increase in crypt multiplicity over time and progress into a tumor and that hyperplastic human ACF can also develop into adenomatous ACF, as reported elsewhere[37,38]. However, this view disagrees with that of other studies[39–41] demonstrating that the degree of dysplasia is not necessarily related to the crypt multiplicity.

Flat ACF

Paulsen *et al.*[42] examined unsectioned methylene blue-stained colon tissues obtained from male F344 rats treated with AOM (sc injection ×2 times, 15 mg/kg body weight), and found two types of early lesions. One was classic elevated ACF, and the other was flat ACF. Classical ACF were seen as enlarged crypts that were elevated from the surrounding epithelium and had elongated luminal openings. However, Paulsen *et al.*[42] described flat ACF as structures that were not elevated. The bright blue appearance and compressed pit pattern of flat ACF were used as criteria for identification.

Flat ACF were characterized by enlarged or small crypts that were not elevated from the epithelium and had round or elongated luminal openings. The investigators also described histological findings of flat ACF with severe dysplasia. In immunohistochemical analysis, classic elevated ACF did not show (0 of 99) cytoplasmic/nuclear expression of the β-catenin protein. In contrast, all flat ACF (8 of 8) displayed cytoplasmic/nuclear expression of the β-catenin protein. The number of classic elevated ACF decreased along with time. Their crypt multiplicity increased during the time period. The number of flat ACF decreased along time, and that of tumors increased correspondingly. The numbers of flat ACF plus tumors were virtually constant. In view of these findings, Paulsen *et al.*[42] concluded that flat ACF display a continuous development from early stages into a tumor.

β-Catenin Accumulated Crypts (BCAC)

In a previous study, we[43] found that focal lesions that display accumulation of the β-catenin protein predispose to carcinogen-induced colon carcinogenesis. We named these lesions β-catenin-accumulated crypts (BCAC) (Fig. 1B). F344 rats were treated with AOM (sc injection ×3 times, 15 mg/kg body weight), and a complete autopsy was performed at 10 weeks after the first AOM treatment[43]. In the topographical view in which colon tissues were stained with methylene blue, we found distinct populations of altered crypts named histologically altered crypts with macroscopically normal-like appearance (HACN) among the tissue samples. In HACN, which are equivalent to BCAC, the *β-catenin* gene was frequently mutated in 10 of 15 samples (67%), and the cytoplasmic β-catenin protein was accumulated in 13 of 15 samples (86%)[43]. Among these lesions, there were ^{28}A→T (Gln→His), ^{29}C→G (Ser→Cys), ^{30}T→C (Tyr→His), ^{32}G→A (Asp→Asn), ^{34}G→A (Gky→Glu), ^{34}G→T (Gly→stop), and ^{41}A→T (Thr→Ile) mutations. Because the lesion in which the β-catenin protein accumulated was considered to be valid in AOM-treated rat colonic mucosa, a time course study was done to examine the status of the protein accumulation, the number of crypts/lesion, and the diameter of the crypts[44]. Both the number of crypts/lesion and the diameter of the β-catenin accumulated crypts that were identified with immunohistochemical analysis significantly increased with the time course[24]. The number of BCAC induced by AOM in AKR/J and SWR/J mice varied by 3–12 per cm^2, and multiplicity was about 3–4 in both strains[24]. Histological abnormality of the crypts and cell proliferation also significantly increased when compared with those of ACF, indicating that BCAC are preneoplastic lesions in AOM-induced colon carcinogenesis[44].

Mucin-depleted Foci (MDF)

Caderni *et al.*[45] identified specific lesions in the colon of rats treated with AOM. When unsectioned colon tissues were stained with high-iron diamine-Alcian blue (HID-AB), foci of crypts with scarce or absent mucins were seen, and such lesions were first defined as mucin-depleted foci (MDF) (Fig. 1C). In that study, male F344 rats received sc injection of AOM (15 mg/kg body weight) twice. The rats developed approximately 4 and 8 MDF/colon at 7 and 15 weeks, respectively, after the start of the experiment, while 271–289 ACF/colon occurred during the same period. Mutations in *β-catenin*, *Apc*, and *K-ras* genes and cytoplasmic β-catenin expression were found in MDF induced by DMH[46–48]. Among these, *β-catenin* gene mutations included ^{32}G→A (Asp→Asn), ^{37}C→T (Ser→Phe), ^{33}C→T (Ser→Phe), and ^{41}C→T (Thr→Ile). In DMH studies, MDF exhibit dysplastic features, and the induction rate of MDF is dose dependent[45,47]. Also, MDF increase in size with time. To examine the multiplicity and distribution of ACF, MDF, and tumors, six-week-old F344 rats were treated with DMH (40 mg/kg body weight sc injection twice a week) followed by 1% dextran sodium sulfate in drinking water. At ten and fourteen weeks after the start of the experiment, animals were euthanized. ACF were mainly found in the middle portion of the colon (Fig. 2A). MDF and tumors occurred more in the distal portion than in the proximal portion (Fig. 2B and C). These results were in accordance with those in the report of Femia *et al*[47]. They found that DMH-induced MDF and tumors were mainly found in the distal portion of the colon, while "classical" ACF were found more predominantly in the middle portion of the colon[47]. Also, Femia *et al.* mentioned that with regard to the ability of ACF/MDF as a biomarker predicting the carcinogenesis status, the heterogeneous nature of each lesion may be related[49].

Only a limited number of findings on MDF are currently available; based on those that are available, Femia and Caderny[27] conclude that MDF are premalignant lesions for colon carcinogenesis and a promising biomarker for study of the effect of chemopreventive agents in colon carcinogenesis. MDF may provide a reliable option as biomarkers for colon carcinogenesis, and it is thought that production or deletion of mucin or both plays some roles in the development of colon tumors. To reiterate, MDF may have both morphological and biochemical aspects as a biomarker. To identify MDF, we[11] demonstrated a simple staining method using 1% Alcian blue (pH 2.5) solution instead of the original HID-AB staining method. In this study, male F344 received sc injections of DMH (40 mg/kg body weight) twice, and the rats developed 19 MDF/colon and 150 ACF/colon at 8 weeks after the start of the experiment. By comparing exact locations of MDF and BCAC on the face-up mucosal samples and by conducting Alcian blue/HE/immunohistochemical staining, we[11] found that MDF are practically identical to BCAC and useful as an early biomarker in rat colon carcinogenesis. In human specimens obtained from patients with colorectal carcinoma (CRC) and familial adenomatous polyposis (FAP), MDF were also identified[50]. The mean numbers of crypts/MDF were 60 and 33 in samples of patients with CRC and FAP, respectively. In a CRC case, the histological diagnosis of MDF was microadenoma with moderate grade dysplasia, while in cases of FAP, the diagnosis was microadenoma with low-grade dysplasia[50]. In a recent

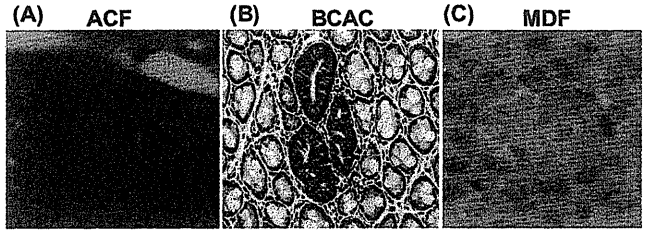

Fig. 1. Topographic views of (A) ACF, (B) BCAC, and (C) MDF. (A) Note that three identical crypts are seen in one focus (methylene blue staining). (B) Crypts with accumulations of β-catenin protein in cytoplasm are present (immunohistochemical staining). (C) A focal lesion characterized by the absence or very small production of mucin (seen as very thin blue-stained crypts) is present (high-iron diamine-Alcian blue staining). ACF, aberrant crypt foci; BCAC, β-catenin accumulated crypts; MDF, mucin-depleted foci.

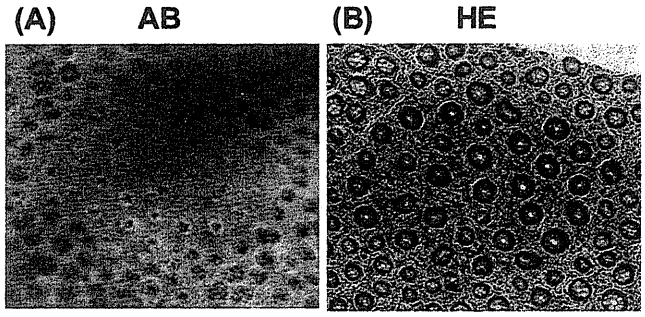

Fig. 3. Topographic views of human MDF stained with (A) 1% Alcian blue (pH 2.5) and (B) hematoxylin and eosin. MDF were identified as focal lesions characterized by loss of Alcian blue staining, attributable to the loss of mucin, as compared with the surrounding normal crypts. AB, Alcian blue; HE, hematoxylin and eosin.

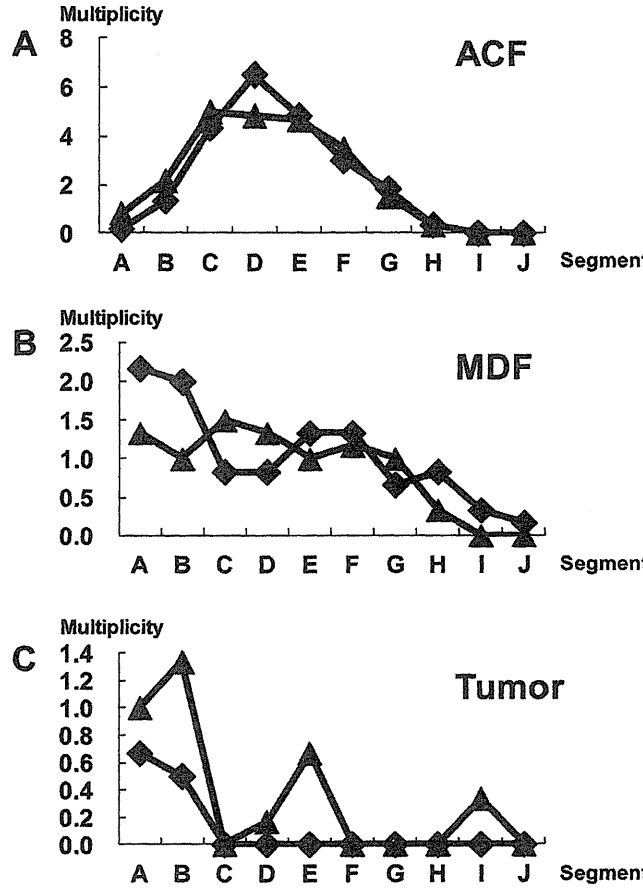

Fig. 2. Distribution of ACF, MDF, and tumors in each segment (A-J) along the colon. The x-axis indicates the segments from the distal to proximal colon. Each segment was named A to J in 2-cm intervals from the anal side. The y-axis indicates the average number of lesions per colon (multiplicity). At ten (closed diamond) and fourteen weeks (closed triangle) after the start of the experiment, animals were euthanized. After fixing of colon tissues with 10% buffered formalin on a filter paper with the mucosal surface up, colon tissues were stained with a 1% solution of Alcian blue, pH 2.5, in 3% acetic acid for 5 min and immediately washed with distilled water. Subsequently, after detection of MDF, the colon tissue was stained with 0.2% methylene blue solution to identify ACF. ACF, MDF, and tumors were noted grossly for their location, number, and size as described earlier[11]. The animal experiment was conducted according to the Institutional Animal Care Guidelines.

study, our group[51] examined human CRC cases and found MDF on the colonic mucosa. The lesion was histologically classified into two categories: flat MDF and protruded MDF. The former lesion did not show nuclear stratification or loss of polarity, but showed Paneth cell metaplasia and decrease/loss of goblet cells, indicative of low-grade dysplasia. Protruded MDF displayed the features of both ACF and MDF, also corresponding to low-grade dysplasia. A topographic view of human MDF is shown in Fig. 3.

Conclusions

This review summarizes topographical, histopathological, and biological features of preneoplastic lesions that have been described in colon carcinogenesis models of the rodent (Table 1). The early lesion has been identified and documented as a preneoplastic lesion in the carcinogenesis process. However, the fact that even the verified lesions appear to contain neoplastic lesions such as a microadenoma indicates the need for further investigation. This may be due to complicated categories or classifications of preneoplastic lesions. Considering the 3R principles (which commonly consist of replacement of methods with no animal use, reduction of the number of test animals, and refinement of methods that minimize the suffering of test animals), a short-term experiment in which an early preneoplastic lesion occurs and can be used as a biomarker should be used to examine toxicity and/or carcinogenicity of test compounds in a specific organ site. In this context, investigators can choose any procedures or methods to examine colonic preneoplastic lesions according to their interests and the objectives of their experiments.

Table 1. Summary of Characters of Preneoplastic Lesions in the Animal Model

Practical name of the lesion	Ref. no. of the current article	Staining method	Features in topographic and/or histological views	
ACF	1, 2, 11, 26, 32	Methelene blue staining	In topographic view, increased cryptial size, thicker epilbelial linig, and increased pericryptical zone.	
		Hematoxylin-eosin (HE) staining	Histological criteria of ACF	
			(1) Non dysplastic foci	Hyercellularity of uniform or normal looking goblet cells with basal-oriented nuclei and apical localization of mucus.
			(2) Mild to moderate dysplastic foci	Hypercellularity of cells with elongated nuclei and focal nuclear stratification.
			(3) Moderate to severe dysplastic foci	Hypercellularity of elongated cells with abundant basophilic cytoplasm. These foci display enlarged and vesiculated nuclei, sometimes with prominent nucleoli.
			Subtype: dysplastic foci	Focal lesions with nuclear stratification, loss of nuclear polarity, structural abnormality of the crypts, Paneth cell metaplasia, a decrease or loss of goblet cells, and presence of mitosis.
Dysplastic ACF	26, 32, 34–36	HE staining	Histologically characterized by distortion of the crypt structure, a decrease in goblet cell number, nuclear stratification, and enlarged nuclei.	
Flat ACF	42	Methelene blue staining	Characterized by bright blue staining, enlarged or small crypts not elevated from the epithelium and round or elongated luminal openings. Because the flat ACF were not observed as elevated structures, their bright blue appearance and compressed pit pattern were used for identification.	
BCAC	24, 43, 44	Immuno-histochemical staining	Accumulation of cytoplasmic β-catenin protein. Crypts of BCAC do not display prominent epithelial cells in a topographic view.	
MDF	11, 45–50	High-iron diamine Alcian blue (HID-AB) staining 1% AB, pH2.5	When colon tissues were stained with HID-AB, foci of crypts with scarce or absent mucin were defined as MDF. MDF can be stained with 1% AB solution.	

ACF, aberrant crypt foci; BCAC, β-catenin accumulated crypts; MDF, mucin-depleted foci.

Acknowledgment: We thank Dr. Tatsuya Kinjo (Department of Digestive and General Surgery, University of the Ryukyus Graduate School of Medicine and Faculty of Medicine, Okinawa, Japan) for valuable comments and discussions. This work was supported in part by a Grant-in-Aid from the Ministry of Education, Culture, Sports, Science and Technology of Japan and a Grant-in-Aid from the Ministry of Health, Labour and Welfare.

References

1. Bird RP. Observation and quantification of aberrant crypts in the murine colon treated with a colon carcinogen: preliminary findings. Cancer Lett. **37**: 147–151. 1987.
2. McLellan EA, and Bird RP. Aberrant crypts: potential preneoplastic lesions in the murine colon. Cancer Res. **48**: 6187–6192. 1988.
3. Tudek B, Bird RP, and Bruce WR. Foci of aberrant crypts in the colons of mice and rats exposed to carcinogens associated with foods. Cancer Res. **49**: 1236–1240. 1989.
4. Roncucci L, Stamp D, Medline A, Cullen JB, and Bruce WR. Identification and quantification of aberrant crypt foci and microadenomas in the human colon. Hum Pathol. **22**: 287–294. 1991.
5. Kristiansen E. The role of aberrant crypt foci induced by the two heterocyclic amines 2-amino-3-methylimidazo[4,5-*f*]quinoline (IQ) and 2-amino-1-methyl-6-phenyl-imidazo[4,5-*b*]pyridine (PhIP) in the development of colon cancer in mice. Cancer Lett. **110**: 187–192. 1996.
6. Bird RP. Role of aberrant crypt foci in understanding the pathogenesis of colon cancer. Cancer Lett. **93**: 55–71. 1995.
7. Morioka T, Suzui M, Nabandith V, Inamine M, Aniya Y, Nakayama T, Ichiba T, Mori H, and Yoshimi N. The modifying effect of *Peucedanum japonicum*, a herb in the Ryukyu Islands, on azoxymethane-induced colon preneoplastic lesions in male F344 rats. Cancer Lett. **205**: 133–141. 2004.
8. Mori Y, Yoshimi N, Iwata H, Tanaka T, and Mori H. The synergistic effect of 1-hydroxyanthraquinone on methylazoxymethanol acetate-induced carcinogenesis in rats. Carcinogenesis. **12**: 335–338. 1991.
9. Chewonarin T, Kinouchi T, Kataoka K, Arimochi H, Kuwahara T, Vinitketkumnuen U, and Ohnishi Y. Effects of roselle (Hibiscus sabdariffa Linn.), a Thai medicinal plant, on the mutagenicity of various known mutagens in Salmonella typhimurium and on formation of aberrant crypt foci induced by the colon carcinogens azoxymethane and 2-amino-1-methyl-6-phenylimidazo[4,5-*b*]pyridine in F344 rats. Food Chem Toxicol. **37**: 591–601. 1999.
10. Sohn OS, Fiala ES, Requeijo SP, Weisburger JH, and Gonzalez FJ. Differential effects of CYP2E1 status on the metabolic activation of the colon carcinogens azoxymethane and

methylazoxymethanol. Cancer Res. **61**: 8435–8440. 2001.
11. Yoshimi N, Morioka T, Kinjo T, Inamine M, Kaneshiro T, Shimizu T, Suzui M, Yamada Y, and Mori H. Histological and immunohistochemical observations of mucin-depleted foci (MDF) stained with Alcian blue, in rat colon carcinogenesis induced with 1,2-dimethylhydrazine dihydrochloride. Cancer Sci. **95**: 792–797. 2004.
12. Morioka T, Suzui M, Nabandith V, Inamine M, Aniya Y, Nakayama T, Chiba T, and Yoshimi N. Modifying effects of Terminalia catappa on azoxymethane-induced colon carcinogenesis in male F344 rats. Eur J Cancer Prev. **14**: 101–105. 2005.
13. Asano N, Kuno T, Hirose Y, Yamada Y, Yoshida K, Tomita H, Nakamura Y, and Mori H. Preventive effects of a flavonoid myricitrin on the formation of azoxymethane-induced premalignant lesions in colons of rats. Asian Pac J Cancer Prev. **8**: 73–76. 2007.
14. Nabandith V, Suzui M, Morioka T, Kaneshiro T, Kinjo T, Matsumoto K, Akao Y, Iinuma M, and Yoshimi N. Inhibitory effects of crude α-mangostin, a xanthone derivative, on two different categories of colon preneoplastic lesions induced by 1, 2-dimethylhydrazine in the rat. Asian Pac J Cancer Prev. **5**: 433–438. 2004.
15. Inamine M, Suzui M, Morioka T, Kinjo T, Kaneshiro T, Sugishita T, Okada T, and Yoshimi N. Inhibitory effect of dietary monoglucosylceramide 1-O-β-glucosyl-*N*-2'-hydroxyarachidoyl-4,8-sphingadienine on two different categories of colon preneoplastic lesions induced by 1,2-dimethylhydrazine in F344 rats. Cancer Sci. **96**: 876–881. 2005.
16. Pretlow TP, Barrow BJ, Ashton WS, O'Riordan MA, Pretlow TG, Jurcisek JA, and Stellato TA. Aberrant crypts: putative preneoplastic foci in human colonic mucosa. Cancer Res. **51**: 1564–1567. 1991.
17. Fenoglio-Preiser CM, and Noffsinger A. Aberrant crypt foci: A review. Toxicol Pathol. **27**: 632–642. 1999.
18. Di Gregorio C, Losi L, Fante R, Modica S, Ghidoni M, Pedroni M, Tamassia MG, Gafà L, Ponz de Leon M, and Roncucci L. Histology of aberrant crypt foci in the human colon. Histopathology. **30**: 328–334. 1997.
19. Nucci MR, Robinson CR, Longo P, Campbell P, and Hamilton SR. Phenotypic and genotypic characteristics of aberrant crypt foci in human colorectal mucosa. Hum Pathol. **28**: 1396–1407. 1997.
20. Shpitz B, Bomstein Y, Mekori Y, Cohen R, Kaufman Z, Neufeld D, Galkin M, and Bernheim J. Aberrant crypt foci in human colons: distribution and histomorphologic characteristics. Hum Pathol. **29**: 469–475. 1998.
21. Osawa E, Nakajima A, and Wada K, ishimine S, Fujisawa N, Kawamori T, Matsuhashi N, Kadowaki T, Ochiai M, Sekihara H, and Nakagama H. Peroxisome proliferator-activated receptor gamma ligands suppress colon carcinogenesis induced by azoxymethane in mice. Gastroenterology. **124**: 361–367. 2003.
22. Steffensen IL, Paulsen JE, Eide TJ, and Alexander J. 2-Amino-1-methyl-6-phenylimidazo[4,5-*b*]pyridine increases the numbers of tumors, cystic crypts and aberrant crypt foci in multiple intestinal neoplasia mice. Carcinogenesis. **18**: 1049–1054. 1997.
23. Shih CK, Chiang W, and Kuo ML. Effects of adlay on azoxymethane-induced colon carcinogenesis in rats. Food Chem Toxicol. **42**: 1339–1347. 2004.
24. Hata K, Yamada Y, Kuno T, Hirose Y, Hara A, Qiang SH, and Mori H. Tumor formation is correlated with expression of β-catenin-accumulated crypts in azoxymethane-induced colon carcinogenesis in mice. Cancer Sci. **95**: 316–320. 2004.
25. Holt PR, Mokuolu AO, Distler P, Liu T, and Reddy BS. Regional distribution of carcinogen-induced colonic neoplasia in the rat. Nutr Cancer. **25**: 129–135. 1996.
26. Papanikolaou A, Wang QS, Papanikolaou D, Whiteley HE, and Rosenberg DW. Sequential and morphological analyses of aberrant crypt foci formation in mice of differing susceptibility to azoxymethane-induced colon carcinogenesis. Carcinogenesis. **21**: 1567–1572. 2000.
27. Femia AP, and Caderni G. Rodent models of colon carcinogenesis for the study of chemopreventive activity of natural products. Planta Med. **74**: 1602–1607. 2008.
28. Lance P, and Hamilton SR. Sporadic aberrant crypt foci are not a surrogate endpoint for colorectal adenoma prevention. Cancer Prev Res (Phila). **1**: 4–8. 2008.
29. Carter JW, Lancaster HK, Hardman WE, and Cameron IL. Distribution of intestine-associated lymphoid tissue, aberrant crypt foci, and tumors in the large bowel of 1,2-dimethylhydrazine-treated mice. Cancer Res. **54**: 4304–4307. 1994.
30. Maskens AP. Histogenesis and growth pattern of 1,2-dimethylhydrazine-induced rat colon adenocarcinoma. Cancer Res. **36**: 1585–1592. 1976.
31. Glauert HP, and Weeks JA. Dose- and time-response of colon carcinogenesis in Fischer-344 rats after a single dose of 1,2-dimethylhydrazine. Toxicol Lett. **48**: 283–287. 1989.
32. Thorup I. Histomorphological and immunohistochemical characterization of colonic aberrant crypt foci in rats: relationship to growth factor expression. Carcinogenesis. **18**: 465–472. 1997.
33. Bird RP, and Pretlow TP. Correspondence re: Giovanna C et al., Effect of dietary carbohydrates on the growth of dysplastic crypt foci in the colon of rats treated with 1,2-dimethylhydrazine. Cancer Res., 51: 3721-3725, 1991. Cancer Res. **52**: 4291–4292. 1992.
34. Ochiai M, Watanabe M, Nakanishi M, Taguchi A, Sugimura T, and Nakagama H. Differential staining of dysplastic aberrant crypt foci in the colon facilitates prediction of carcinogenic potentials of chemicals in rats. Cancer Lett. **220**: 67–74. 2005.
35. Ochiai M, Ushigome M, Fujiwara K, Ubagai T, Kawamori T, Sugimura T, Nagao M, and Nakagama H. Characterization of dysplastic aberrant crypt foci in the rat colon induced by 2-amino-1-methyl-6-phenylimidazo[4,5-*b*]pyridine. Am J Pathol. **163**: 1607–1614. 2003.
36. Paulsen JE, Steffensen IL, Loberg EM, Husoy T, Namork E, and Alexander J. Qualitative and quantitative relationship between dysplastic aberrant crypt foci and tumorigenesis in the Min/+ mouse colon. Cancer Res. **61**: 5010–5015. 2001.
37. Kristiansen E, Thorup I, and Meyer O. Influence of different diets on development of DMH-induced aberrant crypt foci and colon tumor incidence in Wistar rats. Nutr Cancer. **23**: 151–159. 1995.
38. Otori K, Sugiyama K, Hasebe T, Fukushima S, and Esumi H. Emergence of adenomatous aberrant crypt foci (ACF) from hyperplastic ACF with concomitant increase in cell proliferation. Cancer Res. **55**: 4743–4746. 1995.

39. McLellan EA, Medline A, and Bird RP. Sequential analyses of the growth and morphological characteristics of aberrant crypt foci: putative preneoplastic lesions. Cancer Res. **51**: 5270–5274. 1991.
40. Yamashita N, Minamoto T, Ochiai A, Onda M, and Esumi H. Frequent and characteristic K-ras activation in aberrant crypt foci of colon. Is there preference among K-ras mutants for malignant progression? Cancer. **75**: 1527–1533. 1995.
41. Pretlow TP, Roukhadze EV, O'Riordan MA, Chan JC, Amini SB, and Stellato TA. Carcinoembryonic antigen in human colonic aberrant crypt foci. Gastroenterology. **107**: 1719–1725. 1994.
42. Paulsen JE, Loberg EM, Olstorn HB, Knutsen H, Steffensen IL, and Alexander J. Flat dysplastic aberrant crypt foci are related to tumorigenesis in the colon of azoxymethane-treated rat. Cancer Res. **65**: 121–129. 2005.
43. Yamada Y, Yoshimi N, Hirose Y, Kawabata K, Matsunaga K, Shimizu M, Hara A, and Mori H. Frequent *β-catenin* gene mutations and accumulations of the protein in the putative preneoplastic lesions lacking macroscopic aberrant crypt foci appearance, in rat colon carcinogenesis. Cancer Res. **60**: 3323–3327. 2000.
44. Yamada Y, Yoshimi N, Hirose Y, Matsunaga K, Katayama M, Sakata K, Shimizu M, Kuno T, and Mori H. Sequential analysis of morphological and biological properties of β-catenin-accumulated crypts, provable premalignant lesions independent of aberrant crypt foci in rat colon carcinogenesis. Cancer Res. **61**: 1874–1878. 2001.
45. Caderni G, Femia AP, Giannini A, Favuzza A, Luceri C, Salvadori M, and Dolara P. Identification of mucin-depleted foci in the unsectioned colon of azoxymethane-treated rats: correlation with carcinogenesis. Cancer Res. **63**: 2388–2392. 2003.
46. Femia AP, Dolara P, Giannini A, Salvadori M, Biggeri A, and Caderni G. Frequent mutation of Apc gene in rat colon tumors and mucin-depleted foci, preneoplastic lesions in experimental colon carcinogenesis. Cancer Res. **67**: 445–449. 2007.
47. Femia AP, Bendinelli B, Giannini A, Salvadori M, Pinzani P, Dolara P, and Caderni G. Mucin-depleted foci have beta-catenin gene mutations, altered expression of its protein, and are dose- and time-dependent in the colon of 1,2-dimethylhydrazine-treated rats. Int J Cancer. **116**: 9–15. 2005.
48. Femia AP, Tarquini E, Salvadori M, Ferri S, Giannini A, Dolara P, and Caderni G. K-ras mutations and mucin profile in preneoplastic lesions and colon tumors induced in rats by 1,2-dimethylhydrazine. Int J Cancer. **122**: 117–123. 2008.
49. Femia AP, Dolara P, and Caderni G. Mucin-depleted foci (MDF) in the colon of rats treated with azoxymethane (AOM) are useful biomarkers for colon carcinogenesis. Carcinogenesis. **25**: 277–281. 2004.
50. Femia AP, Giannini A, Fazi M, and Tarquini E. salvadori M, Roncucci L, Tonelli F, and Dolara P, Caderni G. Identification of mucin depleted foci in the human colon. Cancer Prev Res (Phila). **1**: 562–567. 2008.
51. Sakai E, Morioka T, Yamada E, Ohkubo H, Higurashi T, Hosono K, Endo H, Takahashi H, Takamatsu R, Cui C, Shinozawa M, Araike M, Samura H, Nishimaki T, Nakajima A, and Yoshimi N. Identification of preneoplastic lesions as mucin-depleted foci in patients with sporadic colorectal cancer. Cancer Sci. **103**: 144–149. 2012.

Promotive effects of cell proliferation and chromosomal instability induced by tribbles-related protein 3 in mouse mammary tumor cells

YUTO SAKAI[1,2], KATSUMI FUKAMACHI[1], MITSURU FUTAKUCHI[1], HIDETOSHI HAYASHI[2] and MASUMI SUZUI[1]

[1]Department of Molecular Toxicology, Nagoya City University Graduate School of Medical Sciences and Medical School, 1 Kawasumi, Mizuho-cho, Mizuho-ku, Nagoya 467-8601; [2]Department of Drug Metabolism and Disposition, Nagoya City University Graduate School of Pharmaceutical Sciences, 3-1 Tanabe-dori, Mizuho-ku, Nagoya 467-8603, Japan

Received January 23, 2013; Accepted March 28, 2013

DOI: 10.3892/or.2013.2441

Abstract. Tribbles-related protein 3 (TRB3) has been shown to be a crucial modulator of tumorigenesis. However, the precise role and the functional morphology of TRB3 are not clearly understood. To elucidate these enigmas we established the cell line, M2TRB3, by introducing the human TRB3 gene and protein in Cl66M2 (M2) mouse mammary tumor cells. This cell line stably expressed the TRB3 gene and protein. After 72 h of cell culture, there was a 34% increase in the growth of M2TRB3 cells compared to the control M2 mock cells. The mean volume of the tumors originating from the M2TRB3 cells was significantly increased by 38% when compared to the mean volume of the M2 mock tumors, and the proliferating cell nuclear antigen (PCNA) labeling index in the M2TRB3 tumors was higher when compared to that of the M2 and M2 mock cells. In the tumor tissue samples, the mean diameter of nuclei in the M2TRB3 tumor cells (9.4±0.3 μm) showed a significant increase compared to that of the M2 mock tumor cells (7.0±0.2 μm). M2TRB3 cells also showed a marked increase in the population of tetraploid or octaploid nuclei compared to M2 mock cells bearing mainly either diploid or tetraploid nuclei. Western blot analysis revealed the overexpression of cyclin B1 and cyclin D1 in M2TRB3 cells when compared to that in the M2 mock cells. These novel findings provide further evidence that TRB3 promotes cell proliferation and chromosomal instability by causing polyploidization during development.

Correspondence to: Dr Masumi Suzui, Department of Molecular Toxicology, Nagoya City University Graduate School of Medical Sciences and Medical School, 1 Kawasumi, Mizuho-cho, Mizuho-ku, Nagoya 467-8601, Japan
E-mail: suzui@med.nagoya-cu.ac.jp

Key words: tribbles-related protein 3, cell proliferation, ploidy, tumor xenograft

Introduction

Tribbles-related protein 3 (TRB3, also known as NIPK, SKIP3) is a mammalian homologue of the *Drosophila Tribbles* gene, and this gene has been identified as an inhibitor of mitosis that regulates cell proliferation, migration and morphogenesis during development (1-3). Among tribbles homologues TRB1, TRB2 and TRB3, TRB3 is the most recently defined family of pseudokinases that contain a serine/threonine kinase catalytic domain but lack an ATP binding site or one of the conserved catalytic motifs essential for kinase activity (4). The interacting partners of TRB3 range from transcription factors, ubiquitin ligase, bone morphogenetic protein (BMP) type II receptor to members of the mitogen-activated protein kinase (MAPK) and phosphoinositide 3-kinase (PI3K) signaling pathways. By interacting with these proteins, it coordinates crucial cellular processes, including glucose/lipid metabolism, apoptosis, adipocyte differentiation, cell stress and regulation of collagen expression (5-9). We previously demonstrated that TRB3 is induced by C/EBP homologous protein (CHOP) and activating transcription factor 4 (ATF4) to regulate their function and endoplasmic reticulum (ER) stress-induced cell death (10) and that TRB3 also regulates the stability of cell division cycle 25A (Cdc25A), an essential activator of cyclin-dependent kinases (CDKs) (11).

Recent studies indicate that the three mammalian tribbles homologues are crucial modulators of tumorigenesis. For instance, both TRB1 and TRB2 are involved in myeloid leukemogenesis (12,13). TRB3 is highly expressed in a wide range of human carcinoma cell lines and in several types of human carcinomas (4,14). However, a precise role of TRB3 in tumorigenesis remains unknown. The aim of the present study was to examine whether the introduction of the human *TRB3* gene into mouse mammary tumor cells affects *in vitro*/*in vivo* growth and chromosomal stability during cell division of tumor cells.

Materials and methods

Cell culture. The human embryonic kidney cell line 293 purchased from the American Type Culture Collection (ATCC,

Manassas, VA, USA) and the human hepatocellular carcinoma cell line HepG2 were cultured in Dulbecco's modified Eagle's medium (DMEM; Wako Pure Chemical Industries, Ltd., Osaka, Japan) supplemented with 10% fetal bovine serum (FBS; Life Technologies, Inc., Rockville, MD, USA) in a humidified incubator with 5% CO_2 at 37°C. The murine mammary tumor cell line Cl66M2 (M2) was generously provided by Dr Rakesh K. Singh (University of Nebraska Medical Center, Omaha, NE, USA) (18) and cultured in DMEM supplemented with 5% FBS in a humidified incubator with 5% CO_2 at 37°C.

Construction of the expression vector. The TRB3 flag-tagged expression vector was constructed by ligating the full length human TRB3 cDNA into *Bam*HI and *Xho*I restriction sites of pcDNA3.1-Hygro (Life Technologies, Inc.) (9). The construct was verified by sequencing.

Preparation of a cell line that stably expresses the TRB3 gene. The expression vector pcDNA3.1-Hygro-flag-human TRB3 was transfected into Cl66M2 cells using Lipofectamine 2000 reagent (Life Technologies, Inc.). This cell line was termed M2TRB3. After transfection, the clone of the cells stably expressing M2TRB3 was selected by a limiting-dilution method in culture media supplemented with hygromycin. The cells transfected with the empty vector were also prepared as the control (M2mock). In M2TRB3 and M2mock cells, the levels of mRNA and protein expression were confirmed by reverse transcription-polymerase chain reaction (RT-PCR) and western blot assays.

In vitro cell proliferation assay. These assays were performed as described previously by us (15). Two murine mammary tumor cell lines M2TRB3 and M2mock were plated into 6-well 35-mm diameter culture plates ($1.0x10^4$ cells/well) in DMEM containing 10% FBS. Cells were starved in DMEM containing 0.5% FBS for 48 h. After starvation, the culture media were removed and cells were grown in DMEM containing 10% FBS for the indicated time course (0-72 h). The cells were washed twice with phosphate-buffered saline (PBS), harvested, resuspended in 1 ml PBS and the number of cells was determined using a hemocytometer Burker-Turk (Erma Inc., Tokyo, Japan). Each assay was repeated more than three times to confirm the results. The number of cells was plotted on a time-response curve as indicated in the figures.

Tumor xenograft assay. Male four-week-old BALB/cSlc-nu/nu mice obtained from Japan SLC, Inc. (Shizuoka Japan) were used. M2, M2TRB3 and M2mock cells ($1.0x10^6$/200 μl) were subcutaneously inoculated into the right lower flank of the mice. Tumor diameters (mm) and body weight (g) were recorded twice weekly. The tumor volume (mm^3) was calculated by the formula: Volume = L x D x H x π/6, where L is the length, D is the depth, and H is the height. At 35 days after inoculation, all mice were euthanized and complete autopsies were performed. Animal experiments were conducted in accordance to the regulations specified by the Institutional Animal Use and Care Committee of Nagoya City University.

Immunohistochemistry and measurement of proliferating cell nuclear antigen (PCNA) labeling index. These assays were performed using an established method as described previously by us (16). Paraffin sections (3-μm) were prepared to include tumors resected from the lower flank of each mouse. These sections were treated in 3% H_2O_2 for 10 min to block the endogenous peroxidase activity. For antigen retrieval, the sections were brought to boiling in 0.1 M citrate buffer, pH 6.0. Sections were incubated with a primary antibody of PCNA (1:500 dilution) (sc-56; Santa Cruz Biotechnology, Inc., Santa Cruz, CA, USA) at room temperature for 60 min. After incubation with the secondary antibody, sections were then stained using an ABC kit (Vector Laboratories, Inc., Burlingame, CA, USA) according to the manufacturer's instructions. The PCNA labeling index was determined by calculating the ratio of PCNA-positive nuclei/total number of nuclei counted. Ten high power fields (x400) per tumor were examined, and >300 cells were counted in each tumor. In M2TRB3 and M2mock tumors, the longest diameter of the nucleus was determined by image analysis using Olympus DP70 system (Olympus Corp., Tokyo, Japan). Four high power fields (x400) per tumor were examined and more than 100 nuclei were counted in each tumor.

Flow cytometric analysis. These assays were performed as previously described (16). M2TRB3 and M2mock cells ($7.5x10^4$ cells/plate) were plated onto 9-cm culture dishes in DMEM plus 10% FBS and grown to yield 50-60% confluence. To synchronize cells at the G0/G1 phase, they were starved by culturing in DMEM plus 0.5% FBS for 48 h. After starvation, cells were then growth in DMEM plus 10% FBS for 72 h. Adherent cells were washed twice with PBS, fixed with 5 ml 70% ethanol, centrifuged, resuspended in 400 μl PBS containing 2 mg/ml RNase (Nacalai Tesque, Inc., Kyoto, Japan), and stained with 400 μl of 0.1 mg/ml propidium iodide (Sigma-Aldrich, St. Louis, MO, USA) in the dark for 30 min or overnight. The cell suspension was filtered through a 60-μm nylon filter (Ikemoto Scientific Technology Co., Ltd., Tokyo). Samples of 10,000-20,000 cells were then analyzed for cell cycle phase distribution and ploidy status using a FACSCalibur™ instrument, and the data were analyzed with the CellQuest computer program (both from Becton-Dickinson, Franklin lakes, NJ, USA) as described in a previous study (16). Cells were harvested just after starvation (0 h) and 72 h after starvation as described in Table I and Fig. 5. Each assay was repeated more than three times to confirm the results.

RT-PCR assays. These assays were conducted using previously established procedures (16). Total RNA was extracted from each cell line grown in 9-cm culture dishes using Isogen (Nippon Gene, Toyama, Japan). The reaction mixture contained 4 μg of total RNA, 1 μl of 10 mM dNTP, 1 μl of random primers (both from Life Technologies, Inc.) and 7 μl of distilled water. The reaction mixture was incubated at 65°C (5 min) for denaturation, chilled on ice for 1 min and 4 μl of 5X RT buffer (Life Technologies, Inc.), 1 μl of 0.1 M dithiothreitol (DTT), 1 μl of the RNaseOut and 1 μl of Superscript® III Reverse Transcriptase (both from Life Technologies, Inc.) were added. After the addition of these reagents, the reaction mixture was incubated at 50°C (60 min) for random primer annealing and 70°C (15 min) for cDNA preparation. One microliter of the reaction mixture was then used for PCR. The primer sequences used in this study were as follows: human TRB3-specific

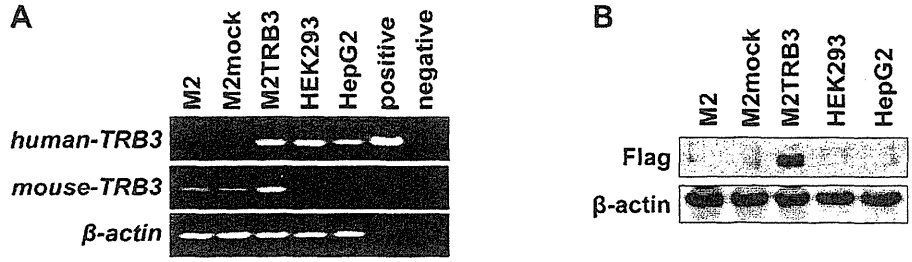

Figure 1. Expression status of exogenous human TRB3 and endogenous mouse TRB3 in the indicated cell lines. (A) Representative results of the RT-PCR analysis. The band in the positive control was derived from DNA fragments that were PCR-amplified using pcDNA3.1-Hygro-flag-human TRB3 vector as a template and the pairs of gene-specific primers listed in Materials and methods. No band was noted in the negative control since the empty vector (pcDNA3.1-Hygro) that does not carry specific sites for the primers was used as a template for PCR. Bands of β-actin were not observed in the positive and negative control samples due to the same reason as the negative control. (B) Representative results of the western blot analysis. The exogenous human TRB3 (Flag) protein was detected in the M2TRB3 cells.

primer set, hTRB3F (5'-CAAGTCGCTCTGAAGGTTCC-3') and hTRB3R (5'-CCATCCTACTCTGGCAAAGC-3'), mouse TRB3-specific primer set, mTRB3F (5'-CAAGTCGCTCT GAAGGTTCC-3') and mTRB3R (5'-CCATCCTACTC TGGCAAAGC-3'), respectively.

β-actin-specific DNA fragments from the same RNA samples were amplified and served as internal controls. Primers actinF (5'-CCGTAAAGACCTCTATGCCAACA-3') and actinR (5'-CGGACTCATCGTACTCCTGCTT-3') were used for amplification of β-actin. PCR was conducted for 26-30 cycles in an iCycler (Bio-Rad Laboratories, Inc., Hercules, CA, USA). Each amplification cycle consisted of 0.5 min at 94°C for denaturation, 0.5 min at 60°C for primer annealing, and 1 min at 72°C for extension. After PCR amplification, the DNA fragments were stained with ethidium bromide and analyzed by 2% agarose gel electrophoresis. The results were confirmed by repeating the experiments.

Western blot assays. These assays were conducted according to previously established procedures (17). The cells were lysed in radioimmunoprecipitation assay (RIPA) buffer [50 mM Tris-HCl (pH 8.0), 150 mM NaCl, 0.1% sodium dodecyl sulfate (SDS), 0.5% deoxycholate, and 1% Triton X-100]. The lysates were subjected to SDS-polyacrylamide gel electrophoresis (PAGE) (12.5%), transferred onto a polyvinylidene difluoride (PVDF) membrane (Immobilon P; Millipore Corp., Bedford, MA, USA) and probed with the antibodies. The primary antibodies used in the present study were anti-β-actin monoclonal antibody (AC-15) (Sigma-Aldrich), anti-cyclin B1 monoclonal antibody (sc-245) (Santa Cruz Biotechnology Inc.), anti-Cdc2 monoclonal antibody (sc-54), anti-Cdk2 polyclonal antibody (sc-163), anti-Cdk4 polyclonal antibody (sc-260), anti-TRB3 polyclonal antibody (sc-34211), anti-cyclin D1 monoclonal antibody (556470; Becton-Dickinson), and anti-Flag monoclonal antibody (018-22381) (Wako Pure Chemical Industries, Ltd.). The immunoreactive proteins were visualized using ImmunoStar Zeta (Wako Pure Chemical Industries, Ltd.) and light emission was quantified with Light Capture (ATTO Corp., Tokyo, Japan). Each assay was repeated more than three times to confirm the results.

Statistical analysis. Differences in the number of cells, tumor volume, PCNA labeling index, and rate of DNA ploidy between cell lines or tumor origins were analyzed by the Student's or Welch's t-test. A value of $P<0.05$ was considered to indicate a statistically significant result.

Results

TRB3 expression in the M2TRB3 cells. To examine the role of TRB3 in cell proliferation, we developed a cell line (M2TRB3) that stably expresses the human *TRB3* gene by transfecting the gene into murine mammary tumor cell line Cl66M2 (M2) (18). We also developed the control cells (M2mock) transfected with empty vector pcDNA3.1-Hygro. M2TRB3 cells expressed both human *TRB3* mRNA and mouse *TRB3* mRNA (Fig. 1A). Human embryonic kidney cell line HEK293 and human hepatoma cell line HepG2 also expressed human *TRB3* mRNA. There was no mRNA expression of human TRB3 in the M2 and M2mock cells. Human TRB3 DNA was PCR-amplified from pcDNA3.1-Hygro-flag-human TRB3 vector and the band was present in the positive lane in Fig. 1A. Expression of the exogenous TRB3 protein (Flag) was present in the M2TRB3 cells. No expression was noted in the protein samples derived from M2, M2mock, HEK293 and HepG2 cells (Fig. 1B). The M2TRB3 and M2mock cells were used for cell proliferation assays.

TRB3 gene enhances cell proliferation and tumor volume. To examine the tumorigenic activity of the TRB3 gene, we investigated its effects on cell and tumor growth using M2TRB3 and M2mock cells. The number of M2TRB3 cells significantly increased compared to M2mock cells at the 48 and 72 h time points ($P<0.01$ and 0.05, respectively) (Fig. 2A). At 72 h, a 34% increase was noted in the number of M2TRB3 cells compared to that of the M2mock cells. To examine the extent of M2TRB3 cell growth when these cells were implanted into the subcutaneous tissue of mice, we used the xenograft mouse model as described in Materials and methods. Twice a week observation was carried out with all mice throughout the experiment. Tumor growth was monitored with the naked eye from day 7 to 35 after inoculation; tumor volume (mm^3) and body weight (g) were measured twice weekly. No specific physical and behavioral changes were noted in any mice. The average volume of the tumors derived from the M2TRB3 cells was significantly increased by 38% when compared with that of the M2mock tumors at experimental day 35 ($P<0.05$) (Fig. 2B).

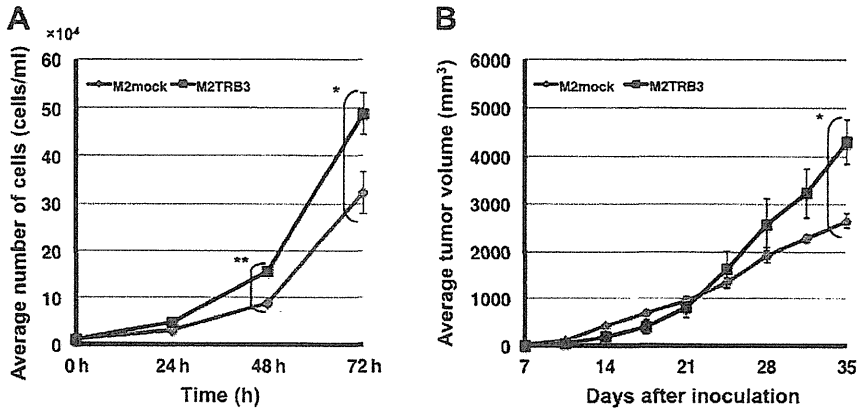

Figure 2. Growth enhancing effects of the TRB3 gene. (A) Growth curve of the cell proliferation assay. Asterisk(s) indicate statistical significance between the two cell lines (*P<0.05, **P<0.01). (B) Volume of the M2TRB3 tumors and M2mock tumors. Asterisk indicates statistical significance in tumor volume between the two tumors (*P<0.05).

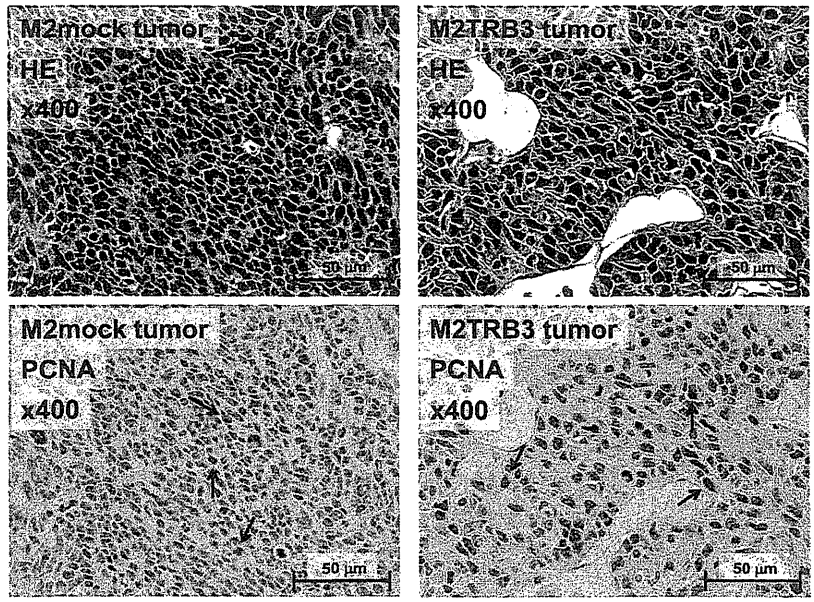

Figure 3. Representative histological features of the M2mock (left rows) and M2TRB3 tumors (right rows). Upper panels were stained with hematoxylin and eosin (HE) and lower panels show immunohistochemical staining of proliferating cell nuclear antigen (PCNA). Approximately 20 and 35% of M2mock and M2TRB3 cells were PCNA-positive (arrows), respectively. Magnification was x400 in all four images.

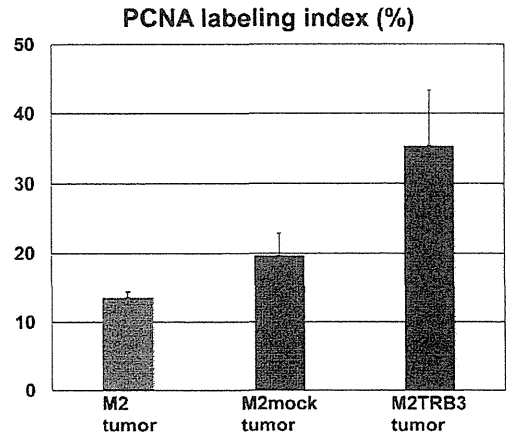

Figure 4. PCNA labeling index in the M2, M2mock and M2TRB tumors. A marked difference was noted between M2mock and M2TRB3 tumors but this difference did not achieve statistical significance.

Gross and histological features and PCNA labeling index of the M2TRB3 tumors. Due to the growth enhancing effects identified above, we aimed to determine whether the TRB3 gene induced morphological changes in tumor tissues. The M2TRB3, M2mock and M2 tumors were excised from the mouse skin, fixed with 10% buffered formalin, and stained with hematoxylin and eosin for histological examination. The tumors were analyzed using a light microscope. M2TRB3 and M2mock tumors presented a pedunculated round shape. Histologically, M2mock tumor cells grew in a solid appearance (Fig. 3, left upper panel). A site of necrosis was present in the central region of the tumor. M2TRB3 tumors were also solid and papillary growth was partially noted (Fig. 3, right upper panel). In the M2TRB3 tumors, the mean diameter of the nucleus (9.4±0.3 μm) was significantly greater than that (7.0±0.2 μm) of the M2mock tumors (P<0.001). The cell proliferation rate was evaluated by measuring the PCNA

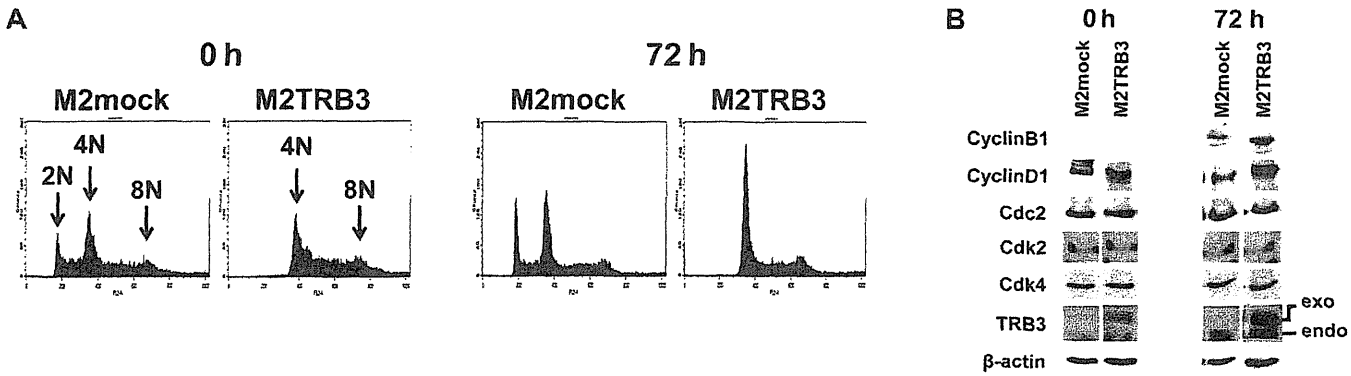

Figure 5. Effects of the TRB3 gene on DNA ploidy and protein expression. (A) Representative results of the flow cytometric analysis. After synchronizing cells in the G0/G1 phase, ploidy status was determined by flow cytometric analysis at 0 (left two panels) and 72 h (right two panels) in the M2mock and M2TRB3 cell lines. Note three peaks (2N, diploid; 4N, tetraploid; 8N, octaploid) in different locations in the DNA histogram. (B) Protein expression status of cell cycle control molecules and TRB3 in M2mock and M2TRB3 cell lines. Cell lysates were extracted at the indicated times (h) of the cell culture and then examined by western blot analysis for the indicated proteins, using the respective antibodies, as described in Materials and methods. β-actin was used as an internal control. Exogenous human TRB3 and endogenous mouse TRB3 are describes as exo and endo, respectively.

Table I. Distribution and rate (%) of ploidy in the M2TRB3 and M2mock cell lines.

		Time (h) after starvation	
Cell line	Ploidy	0 h	72 h
M2mock	2N	12.1±0.3[a]	16.6±0.1[b]
M2TRB3	2N	0.0±0.0	0.0±0.0
M2mock	4N	37.0±0.1	38.5±0.2[b]
M2TRB3	4N	41.6±2.5	57.5±0.5
M2mock	8N	6.0±0.1[a]	3.5±0.0[b]
M2TRB3	8N	25.3±1.8	16.2±0.3

Differences in the percentage of ploidy in M2TRB3 and M2mock cell lines. M2TRB3 vs. M2mock, [a]P<0.01 and [b]P<0.001.

labeling index as described in Materials and methods. The PCNA labeling index of the M2TRB3 tumors was higher than that of the M2 and M2mock tumors but this difference was not statistically significant (Fig. 3 lower panels and Fig. 4).

TRB3 affects the ploidy distribution of mouse mammary tumor cells. Due to the differences in tumor morphology noted in Fig. 3, we examined the effects of the TRB3 gene on DNA ploidy in M2mock and M2TRB3 cells. After synchronizing cells in the G0/G1 phase, we conducted experiments at 0 and 72 h using flow cytometric analysis. Representative DNA histograms of the analysis for these cells are shown in Fig. 5A, and distribution and rate of DNA ploidy are shown in Table I. In M2mock cells, the average percentage of diploid nuclei measured 12-16%. In contrast, no diploid nuclei were observed in M2TRB3 cells (Table I and Fig. 5A, far right panels). M2TRB3 cells showed a significant increase by 19 and 12% in the population of octaploid nuclei at 0 and 72 h, respectively, when compared to M2mock cells (Table I). There was also an increase (4-19%) in the population of tetraploid nuclei in the M2TRB3 cells. These results indicate that TRB3 affects the status of DNA ploidy in mouse mammary tumor cells. M2mock cells exhibited population peaks of aneuploid nuclei (2N, 4N and 8N), indicating that these cells harbor a variable number of chromosomes.

Expression status of TRB3 and cell cycle control molecules in M2TRB3 and M2mock cells. Due to the growth enhancing effects of TRB3 as noted in Fig. 2 and nuclear hyperploidy in M2TRB3 cells, we examined whether these cells affected the levels of expression of TRB3 and cell cycle control molecules. Thus, we measured the protein expression levels of TRB3 and cell cycle control molecules cyclin B1, cyclin D1, Cdc2, Cdk2 and Cdk4. In M2TRB3 cells, both exogenous and endogenous TRB3 were highly expressed at 72 h compared to M2mock cells that only expressed endogenous TRB3 (Fig. 5B, right two columns). In contrast, a weak expression level of endogenous TRB3 was observed at 0 h in the M2mock cells, and marginal expression was noted in both exogenous and endogenous TRB3 at the same time point in these cells. Cyclin B1 and cyclin D1 expression levels in the M2TRB3 cells increased at 72 h of the cell culture, in which tumor cells were out of synchrony, compared to those of the M2mock cells (Fig. 5B). Expression levels of Cdc2, Cdk2, and Cdk4 showed no change between the M2TRB3 and M2mock cells.

Discussion

Several human tumor tissues have recently been shown to highly express TRB3 mRNA (14). It has also been demonstrated by us that TRB3 regulates the stability of Cdc25A, an essential activator of CDKs (10). However, the precise role and functional morphology of TRB3 have not been established yet. Thus, we carried out the present study to provide further evidence concerning cell growth and morphological changes in mouse mammary tumor cells by focusing on the expression levels of TRB3 and cell cycle control molecules, cellular nucleus size, and the status of DNA ploidy. M2TRB3 cells showed a significant numerical increase compared to the control M2mock cells. As a result, the doubling time of the M2TRB3 and M2mock cell lines was approximately 12

and 15 h, respectively (Fig. 2A). A similar condition was also observed in the tumors, clearly indicating that in this context TRB3 had an enhancing property on the growth of mouse mammary tumor cells.

It is well understood that cell volume increases with DNA ploidy, and this correlation has been observed in a wide variety of eukaryotic cells (19). Increased DNA ploidy can exert its effects by increasing nuclear size, chromatin content, and the expression levels of a certain gene (19). We found that in the M2TRB3 tumors the mean diameter of the nucleus measured 9.4±0.3 μm and that of the M2mock tumors was 7.0±0.2 μm. From the flow cytometric analysis we also found a significant increase in the population of M2TRB3 cells bearing tetraploid or octaploid nuclei compared to that of the M2mock cells bearing mostly diploid or tetraploid nuclei (Fig. 5A). These findings are consistent with those reported by Danielsen *et al* (20) who demonstrated that nuclei of 6.0-7.5 μm in diameter are classified as diploid, 7.5-9.0 μm as tetraploid, and 9.5-11.0 μm as octaploid. Collectively, TRB3 may have the ability of polyploidization during development.

Cyclins are the key molecules in cell cycle control due to their specific and periodic expression during cell cycle progression. Cyclin D1 complexes with Cdk4 and Cdk6 and thereby regulates transition from the G1 phase into the S phase by phosphorylation and inactivation of pRB (21-24). Phosphorylation causes release of the transcription factor E2F that promotes mitosis (24,25). Gene amplification and/or protein overexpression of cyclin D1 occurs in a variety of human carcinomas and tumors in animal models (26,27). Unlike cyclin D1, the activity of cyclin B1 is essential for G2/M phase of the cell cycle through a complex with Cdc2 (28). However, little is known about the association between DNA ploidy and cyclin B1/cyclin D1 expression status. We found elevated expression levels of cyclin B1 and cyclin D1 in M2TRB3 cells without significant changes in expression levels of Cdc2, Cdk2 and Cdk4 (Fig. 5B). Furthermore, M2TRB3 cells totally lack diploid nuclei but a population of the M2mock cells consisted mainly of diploid or tetraploid nuclei, suggesting that expression of cyclin B1 and cyclin D1 may positively correlate with the generation of hyperploid nuclei and thereby further promote the chromosomal instability in TRB3-overexpressing cells. Similar results regarding cyclin B1/D1 overexpression and promotion of tetraploidy or aneuploidy (>2N) were previously obtained in human breast carcinoma and mouse myeloid cells (28,29). As we found in the present study, the novel aspect of the TRB3 gene is that this gene induces an increase in cell proliferation and polyploidy leading to enlargement of the nuclear size of the implanted mouse mammary tumor cells. These effects of TRB3 may cause chromosomal instability. The detailed mechanism of this chromosomal instability is not known but may be related to the above-described effects of TRB3 on morphological function. In a recent study, we demonstrated that TRB3 may regulate the activity of anaphase-promoting complex/cyclosome (APC/C^{Cdh1}) that is a major ubiquitin ligase complex regulating the progression of the cell cycle through the ubiquitination and subsequent degradation of cell cycle control molecules including cyclin B1 (30,31). In the present study, we found an elevated expression level of the cyclin B1 protein in M2TRB3 cells that overexpressed the human TRB3 gene. We should emphasize that two cell lines M2TRB3 and M2mock differ in synchrony status that may influence their response to morphological function. This intriguing respect may also reflect the role of cell cycle progression of TRB3. Thus, it is of interest to examine whether the TRB3 gene causes *de novo* morphological changes leading to tumorigenesis in a specific organ site. An additional study using the TRB3 transgenic animal model is currently in progress to answer this question.

Acknowledgements

We thank Dr Hiroyuki Tsuda for the valuable comments and discussions. We also acknowledge the excellent technical assistance of Kenta Moriwaki and Shuhei Ikenaga. This study was supported by a Grant-in-Aid from the Ministry of Education, Culture, Sports, Science, and Technology, and the Ministry of Health, Labour, and Welfare of Japan.

References

1. Grosshans J and Wieschaus E: A genetic link between morphogenesis and cell division during formation of the ventral furrow in *Drosophila*. Cell 101: 523-531, 2000.
2. Mata J, Curado S, Ephrussi A and Rørth P: Tribbles coordinates mitosis and morphogenesis in *Drosophila* by regulating string/CDC25 proteolysis. Cell 101: 511-522, 2000.
3. Seher TC and Leptin M: Tribbles, a cell-cycle brake that coordinates proliferation and morphogenesis during *Drosophila* gastrulation. Curr Biol 10: 623-629, 2000.
4. Bowers AJ, Scully S and Boylan JF: SKIP3, a novel *Drosophila* tribbles ortholog, is overexpressed in human tumors and is regulated by hypoxia. Oncogene 22: 2823-2835, 2003.
5. Bezy O, Vernochet C, Gesta S, Farmer SR and Kahn CR: TRB3 blocks adipocyte differentiation through the inhibition of C/EBPβ transcriptional activity. Mol Cell Biol 27: 6818-6831, 2007.
6. Chan MC, Nguyen PH, Davis BN, Ohoka N, Hayashi H, Du K, Lagna G and Hata A: A novel regulatory mechanism of the bone morphogenetic protein (BMP) signaling pathway involving the carboxyl-terminal tail domain of BMP type II receptor. Mol Cell Biol 27: 5776-5789, 2007.
7. Du K, Herzig S, Kulkarni RN and Montminy M: TRB3: a tribbles homolog that inhibits Akt/PKB activation by insulin in liver. Science 300: 1574-1577, 2003.
8. Qi L, Heredia JE, Altarejos JY, Screaton R, Goebel N, Niessen S, Macleod IX, Liew CW, Kulkarni RN, Bain J, Newgard C, Nelson M, Evans RM, Yates J and Montminy M: TRB3 links the E3 ubiquitin ligase COP1 to lipid metabolism. Science 312: 1763-1766, 2006.
9. Tang M, Zhong M, Shang Y, Lin H, Deng J, Jiang H, Lu H, Zhang Y and Zhang W: Differential regulation of collagen types I and III expression in cardiac fibroblasts by AGEs through TRB3/MAPK signaling pathway. Cell Mol Life Sci 65: 2924-2932, 2008.
10. Ohoka N, Yoshii S, Hattori T, Onozaki K and Hayashi H: TRB3, a novel ER stress-inducible gene, is induced via ATF4-CHOP pathway and is involved in cell death. EMBO J 24: 1243-1255, 2005.
11. Sakai S, Ohoka N, Onozaki K, Kitagawa M, Nakanishi M and Hayashi H: Dual mode of regulation of cell division cycle 25 A protein by TRB3. Biol Pharm Bull 33: 1112-1116, 2010.
12. Jin G, Yamazaki Y, Takuwa M, Takahara T, Kaneko K, Kuwata T, Miyata S and Nakamura T: Trib1 and Evi1 cooperate with Hoxa and Meis1 in myeloid leukemogenesis. Blood 109: 3998-4005, 2007.
13. Keeshan K, He Y, Wouters BJ, Shestova O, Xu L, Sai H, Rodriguez CG, Maillard I, Tobias JW, Valk P, Carroll M, Aster JC, Delwel R and Pear WS: Tribbles homolog 2 inactivates C/EBPα and causes acute myelogenous leukemia. Cancer Cell 10: 401-411, 2006.
14. Xu J, Lv S, Qin Y, Shu F, Xu Y, Chen J, Xu BE, Sun X and Wu J: TRB3 interacts with CtIP and is overexpressed in certain cancers. Biochim Biophys Acta 1770: 273-278, 2007.

15. Suzui M, Sunagawa N, Chiba I, Moriwaki H and Yoshimi N: Acyclic retinoid, a novel synthetic retinoid, induces growth inhibition, apoptosis, and changes in mRNA expression of cell cycle- and differentiation-related molecules in human colon carcinoma cells. Int J Oncol 28: 1193-1199, 2006.
16. Suzui M, Inamine M, Kaneshiro T, Morioka T, Yoshimi N, Suzuki R, Kohno H and Tanaka T: Indole-3-carbinol inhibits the growth of human colon carcinoma cells but enhances the tumor multiplicity and volume of azoxymethane-induced rat colon carcinogenesis. Int J Oncol 27: 1391-1399, 2005.
17. Suzui M, Masuda M, Lim JT, Albanese C, Pestell RG and Weinstein IB: Growth inhibition of human hepatoma cells by acyclic retinoid is associated with induction of p21(CIP1) and inhibition of expression of cyclin D1. Cancer Res 62: 3997-4006, 2002.
18. Futakuchi M, Nannuru KC, Varney ML, Sadanandam A, Nakao K, Asai K, Shirai T, Sato SY and Singh RK: Transforming growth factor-beta signaling at the tumor-bone interface promotes mammary tumor growth and osteoclast activation. Cancer Sci 100: 71-81, 2009.
19. Jorgensen P and Tyers M: How cells coordinate growth and division. Curr Biol 14: 1014-1027, 2004.
20. Danielsen H, Lindmo T and Reith A: A method for determining ploidy distributions in liver tissue by stereological analysis of nuclear size calibrated by flow cytometric DNA analysis. Cytometry 7: 475-480, 1986.
21. Hunter T and Pines J: Cyclins and cancer. II: cyclin D and CDK inhibitors come of age. Cell 79: 573-582, 1994.
22. Weinberg RA: The retinoblastoma protein and cell cycle control. Cell 81: 323-330, 1995.
23. Chellappan SP, Hiebert S, Mudryj M, Horowitz JM and Nevins JR: The E2F transcription factor is a cellular target for the RB protein. Cell 65: 1053-1061, 1991.
24. Wilson CS, Butch AW, Lai R, Medeiros LJ, Sawyer JR, Barlogie B, McCourty A, Kelly K and Brynes RK: Cyclin D1 and E2F-1 immunoreactivity in bone marrow biopsy specimens of multiple myeloma: relationship to proliferative activity, cytogenetic abnormalities and DNA ploidy. Br J Haematol 112: 776-782, 2001
25. Johnson DG, Schwarz JK, Cress WD and Nevins JR: Expression of transcription factor E2F1 induces quiescent cells to enter S phase. Nature 365: 349-352, 1993.
26. Staibano S, Lo Muzio L, Pannone G, Mezza E, Argenziano G, Vetrani A, Lucariello A, Franco R, Errico ME and De Rosa G: DNA ploidy and cyclin D1 expression in basal cell carcinoma of the head and neck. Am J Clin Pathol 115: 805-813, 2001.
27. Bartkova J, Lukas J, Strauss M and Bartek J: Cyclin D1 oncoprotein aberrantly accumulates in malignancies of diverse histogenesis. Oncogene 10: 775-778, 1995.
28. Collecchi P, Santoni T, Gnesi E, Giuseppe Naccarato A, Passoni A, Rocchetta M, Danesi R and Bevilacqua G: Cyclins of phases G1, S and G2/M are overexpressed in aneuploid mammary carcinomas. Cytometry 42: 254-260, 2000.
29. Yin XY, Grove L, Datta NS, Katula K, Long MW and Prochownik EV: Inverse regulation of cyclin B1 by c-Myc and p53 and induction of tetraploidy by cyclin B1 overexpression. Cancer Res 61: 6487-6493, 2001.
30. Ohoka N, Sakai S, Onozaki K, Nakanishi M and Hayashi H: Anaphase-promoting complex/cyclosome-cdh1 mediates the ubiquitination and degradation of TRB3. Biochem Biophys Res Commun 392: 289-294, 2010.
31. Lukas C, Sørensen CS, Kramer E, Santoni-Rugiu E, Lindeneg C, Peters JM, Bartek J and Lukas J: Accumulation of cyclin B1 requires E2F and cyclin-A-dependent rearrangement of the anaphase-promoting complex. Nature 401: 815-818, 1999.